Received: 12 February 2020 | Revised: 27 October 2020 | Accepted: 30 November 2020

DOI: 10.1002/eqe.3409

RESEARCH ARTICLE

WILEY

Integral abutment bridges: Investigation of seismic soil-structure interaction effects by shaking table testing

Gabriele Fiorentino[1] | **Cihan Cengiz**[2] | **Flavia De Luca**[2] | **George Mylonakis**[2,7,8] | **Dimitris Karamitros**[2] | **Matt Dietz**[2] | **Luiza Dihoru**[2] | **Davide Lavorato**[1] | **Bruno Briseghella**[3] | **Tatjana Isakovic**[4] | **Christos Vrettos**[5] | **Antonio Topa Gomes**[6] | **Anastasios Sextos**[2] | **Camillo Nuti**[1,3]

[1] Department of Architecture, Roma Tre University, Rome, Italy

[2] Department of Civil Engineering, University of Bristol, Bristol, UK

[3] College of Civil Engineering, Fuzhou University, Fuzhou, China

[4] Faculty of Civil and Geodetic Engineering, University of Ljubljana, Ljubljana, Slovenia

[5] Department of Civil Engineering, Technical University Kaiserslautern, Kaiserslautern, Germany

[6] Department of Civil Engineering, University of Porto, Porto, Portugal

[7] Department of Civil and Infrastructure Engineering, Khalifa University, Abu Dhabi, UAE

[8] Department of Civil and Environmental Engineering, University of California at Los Angeles (UCLA), Los Angeles, California

Correspondence
Flavia De Luca, Department of Civil Engineering, University of Bristol, Bristol, United Kingdom.
Email: flavia.deluca@bristol.ac.uk

Funding information
EU H2020, Grant/Award Number: 730900; National Natural Science Foundation of China, Grant/Award Number: 51778148

Abstract

In recent years there has been renewed interest on integral abutment bridges (IABs), mainly due to their low construction and maintenance cost. Owing to the monolithic connection between deck and abutments, there is strong soil-structure interaction between the bridge and the backfill under both thermal action and earthquake shaking. Although some of the regions where IABs are adopted qualify as highly seismic, there is limited knowledge as to their dynamic behaviour and vulnerability under strong ground shaking. To develop a better understanding on the seismic behaviour of IABs, an extensive experimental campaign involving over 75 shaking table tests and 4800 time histories of recorded data, was carried out at EQUALS Laboratory, University of Bristol, under the auspices of EU-sponsored SERA project (Seismology and Earthquake Engineering Research Infrastructure Alliance for Europe). The tests were conducted on a 5 m long shear stack mounted on a 3 m × 3 m 6-DOF earthquake simulator, focusing on interaction effects between a scaled bridge model, abutments, foundation piles and backfill soil. The study aims at (a) developing new scaling procedures for physical modelling of IABs, (b) investigating experimentally the potential benefits of adding compressible inclusions (CIs) between the abutment and the backfill and (c) exploring the influence of different types of connection between the abutment and the pile foundation. Results indicate that the CI reduces the accelerations on the bridge deck and the settlements in the backfill, while disconnecting piles from the cap decreases bending near the pile head.

KEYWORDS
compressible inclusion, integral abutment bridges, pile-to-cap connection, shaking table testing, soil structure interaction

1 | INTRODUCTION

Bridges represent the largest investment and the most vulnerable element in transportation networks.[1–4] Their functionality is crucial both under working conditions and after rare events such as strong earthquakes. In seismic regions, bridges are often designed as statically determined systems using bearing supports and expansion joints between the girder, the piers and the abutments. This allows for bridge movements due to gravity, thermal gradients, traffic and dynamic loads, yet forces the joints to undergo cyclic motions which, in turn, require expensive routine maintenance. Extensive damage to bridges, including pounding and unseating of decks at the joints, has been observed in the aftermath of strong earthquakes.[5,6]

Integral abutment bridges (IABs) provide an alternative design approach characterised by a monolithic connection between the deck and the abutments. From a structural point of view, the use of a monolithically cast frame superstructure has several advantages over traditional designs such as reduced sagging moment at mid-span, smaller girders and smaller intermediate supports.[7,8] Furthermore, these designs are characterised by improved durability (i.e., reduced corrosion and material degradation at the joints), lower costs associated with construction and maintenance[9] and improved driving comfort. On the other hand, thermal and lateral loads induce high stresses in the structure due to the rigidity of the deck-abutment connection.[10] Depending on bridge length, the absence of expansion joints to accommodate creep, shrinkage, and thermally induced cyclic loading, may cause significant fatigue-related distress on the piles[11] as well as densification in the backfill.[12] Moreover, the monolithic rigid frame design of the IABs may lead to strong bridge-abutment-backfill interaction under seismic loading.

IABs have received increasing attention by designers in recent times and are widely used in many countries for small- to medium-span highway bridges and overcrossings.[13] They constitute a significant part of the transportation infrastructure stock with an estimated number in service in excess of 9000 in the United States alone.[14,15] The technique is becoming increasingly popular in Sweden, United Kingdom and Japan,[16] while designs vary according to practices and requirements outlined by local transportation agencies. For instance, in the UK the design often involves spread footings and embedded abutments, whereas in the rest of Europe a range of pile configurations are employed. In the United States a single line of H-piles is typically used to support abutments.[17,18] Currently, the design of long-span integral abutment bridges is limited to conservative maximum lengths due to a lack of available design guidance.[19–22,11] In the UK, the design provisions restrict the spans to 60 m and limit the skewness to 30°,[23] even though the bridges are not designed for earthquake loads.

Given the economic viability and widespread use of IABs, their mechanical behaviour should be thoroughly investigated under both static and dynamic loads. To this end, there is a clear need for developing know-how as to IAB-soil interaction to feed relevant research findings into design code development.[24] Some national codes and guidelines offer provisions for the static design of IABs.[25–27] On the other hand, in earthquake-prone areas in Europe such as Italy and Greece, the use of IABs is limited mainly due to a lack of explicit design guidelines for seismic loads (e.g., no explicit clauses are provided in the Eurocodes), but also due to a shortage in dependable mechanistic models to predict their response.

With reference to soil-structure interaction (SSI), the response of deck, abutments and embankments is strongly coupled: inertial actions are transmitted from the girder to the abutments which, in turn, are in contact with the embankments. Passive earth pressures acting on abutments can help resist earthquake forces, but may also act as a destabilising force.[28,29] Seismic actions could also cause an abrupt increase in forces and an irreversible build-up of lateral earth pressures.[30] In this light, some authors have proposed the use of compressible inclusions (CIs), such as expanded polystyrene (EPS) geofoam, to be interposed between the abutments and the backfill to mitigate earth pressures and uncouple the response of the bridge from that of the backfill.[31–34,11]

In order to investigate their response to earthquakes, structural monitoring was carried out in the 1990s on American highway overcrossings in earthquake prone areas. The monitoring of two-span integral abutment overcrossings in California quantified the dynamic contribution of embankments and showed that the natural frequency and damping of the soil-structure system are sensitive to the intensity of ground motion.[35] It was also observed that even if the superstructure remains linear, which is anticipated in IABs, local nonlinear material behaviour in the backfill could result in nonlinearity in the entire soil-bridge system.[36] Based on these early studies, various mechanistic models have been proposed for the numerical modelling of relevant SSI effects.[37–40] However, there is a notable lack of know-how to address a wide range of bridge systems and soil conditions, since seismic response of IABs is governed by a series of complex, interdependent mechanisms. As the monolithic frames are designed to resist moments, one of the locations to look for seismically induced damage is the connection between the superstructure and the abutment.[41] Although post-earthquake investigations have clearly shown that IABs suffer less structural damage than conventional bridges,[42] in cases where appreciable damage

has occurred this is usually confined to the abutment walls and the piles. As the backfill is subjected to recurrent cyclic traffic loads during IAB's operation, the soil material is further compacted, and the lateral earth pressures exerted on the abutment wall grow. This effect is aggravated when seismically induced loads cause a further densification and subsequent increase in lateral thrusts. Post-earthquake reconnaissance studies in New Zealand following the 2010 Darfield, 2011 Christchurch, 2013 Cook Strait and 2013 Lake Grassmere earthquakes have revealed damage patterns on the lateral earth pressure bearing elements.[42]

With reference to boundary conditions, the presence of CIs between the abutment and the backfill allows dissipation of lateral earth pressures. In some early applications inclusions of this type were employed against static loads,[43,44] while more recently their use was extended to earthquake induced earth pressures against rigid walls.[33,45–47] Moreover, CIs allow for controlling displacements of the backfill which can be used in performance-based design.[48,49]

Based on 1-g shaking table tests on a 1-m high geofoam isolated rigid retaining wall, Bathurst et al[45] observed that CIs reduce dynamic earth pressure loads by about 15-40% depending mainly on the density of the geofoam buffer. Up to a 50% reduction in dynamic lateral earth pressure for flexible cantilever earth retaining walls has also been reported in a recent experimental study by Ertugrul et al.[47] Similar 1-g shaking table tests carried out by Reddy and Krishna[50] exhibited even higher reductions (by about 70-80%). Such reductions were achieved by adding shredded tire chips behind the wall.

Experimental investigations of SSI with a focus on the potentially beneficial/detrimental role of integral abutments on seismic response are rare. Quarter scale two-span and four-span bridge models were tested at the University of Nevada at Reno,[51] while shaking table tests exploring the abutment contribution to the dynamic bridge response were conducted at the University of California in San Diego.[52]

Motivated by the limited knowledge in the subject, an extensive experimental campaign, involving over 75 tests on a scaled, IAB model, was conducted at the Earthquake Engineering Laboratory (EQUALS), University of Bristol (UoB), as part of the EU-funded project SERENA, under the auspices of the EU-SERA transnational access research project.[53,54] The tests were designed to investigate the earthquake response of IABs and associated SSI effects between the bridge, the backfill, the abutments and the pile foundation. The main objectives of the project are discussed in section 2, followed by a description of the experimental configuration (section 3). The design of the physical model and its scaling is discussed in section 4. Sections 5 and 6 present experimental results and a set of conclusions.

The novel set of shaking table tests reported in this article focus on exploring the potential benefits stemming from the use of CIs and non-moment resisting pile-to-cap connections in different combinations, with emphasis on SSI. One of the main challenges addressed herein is the scaling of the SSI problem to fit the laboratory capabilities (size-wise), without compromising similitude to furnish results that can be employed in design of real bridges. The aim of the study is to reduce the epistemic uncertainty associated with IAB dynamics and provide experimental data to support development of design guidelines for bridges of this type.

2 | SERENA PROJECT

The focus of the herein reported tests is to explore: (a) the earthquake response of IABs including dynamic earth pressures on the abutment walls and bending of the piles supporting the abutments, (b) ways of minimising the associated demands using pertinent design solutions such as disconnecting the pile heads from the cap and the abutments from the backfill through installation of CIs and (c) induced settlements due to dynamic condensation of the backfill.

The design of the model was constrained by the dimensions of the shear stack, the need to avoid boundary effects and the necessity to ensure symmetry and facilitate the interpretation of the results. To this end, a single-span model with flexible abutments was adopted. The foundation has a double row of piles which is a rational design approach in seismic regions, although in the United States the trend is to have only one pile row.[13] A novel approach using different scaling factors for the deck and the abutment is developed, as described in the following. The main goal is to preserve the relative stiffness proportions between the structure and the soil, to realistically model the relevant SSI effects. Based on a set of IAB prototypes available in literature[55,15,21,22,56,96], some general features of a representative prototype were adopted (Figure 1). In the herein reported experiments, the central part of the bridge, including the pier at mid-span, is not explicitly modelled. Moreover, some additional simplifications had to be accepted. Specifically: (a) the backfill surface lies at a different elevation with respect to the deck; (b) the approaching slab, usually present in actual bridges, was not realised in the model; (c) the cross-sections of the deck beams employed are not representatives of specific prototype bridge sections, but were selected to model a variety of configurations including single- and multi-span designs.

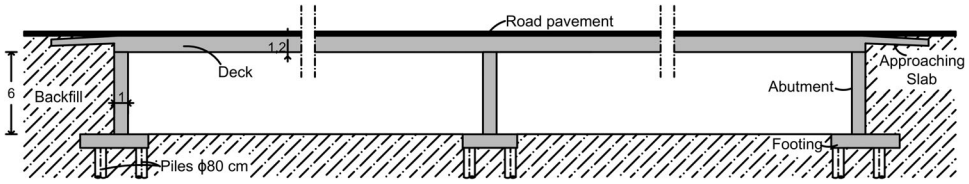

FIGURE 1 Example of double-span integral bridge (dimensions in meters)

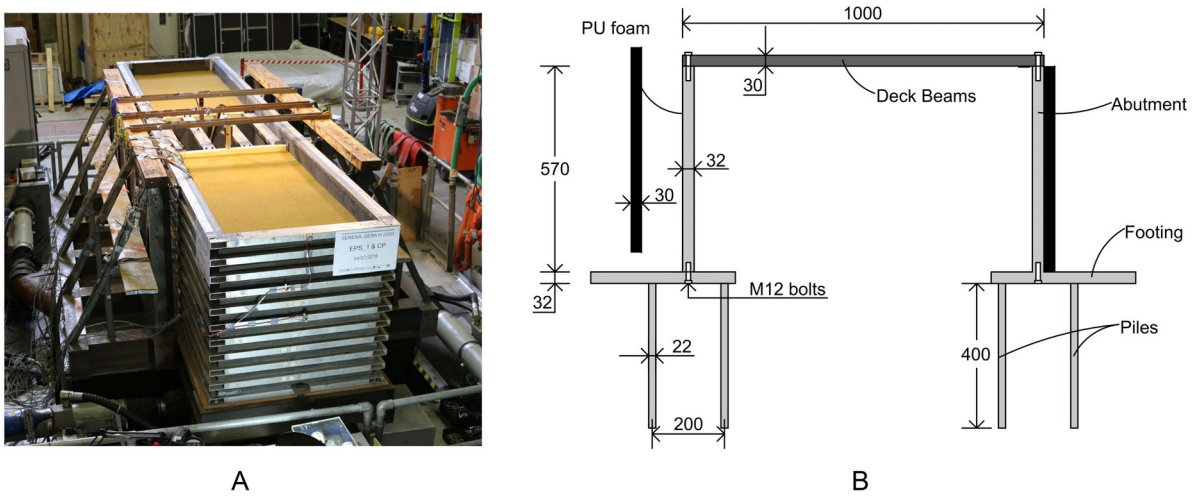

FIGURE 2 A, Integral Bridge model inside the shear stack of EQUALS, University of Bristol, filled with sand; B, section of the bridge model. All dimensions are in mm

3 | EQUIPMENT, MATERIALS AND TEST CONFIGURATIONS

3.1 | Earthquake simulator

The 6-DOF earthquake simulator (ES) of the Earthquake and Large Structures Laboratory (EQUALS) at University of Bristol was employed for the experimental campaign. The ES consists of a 3 m × 3 m cast aluminium platform weighing 3.8 tons, is capable of carrying a maximum payload of 15 tons. The ES is referred in the ensuing to as the 'shaking table'. The ES is driven by eight hydraulic actuators (four horizontal and four vertical) with a dynamic capacity of 70 kN each and a maximum stroke of 300 mm. The ES is capable of providing accelerations of up to 1.2 g (vertically) and up to 1.6 g (horizontally) for 10 tons of payload. Its frequency operating range is 0-100 Hz.

3.2 | Specimen geometry and configurations

Scaled physical models consisting of piles, abutment footings and walls, bridge deck, foundation and backfill soil were installed in the large equivalent shear beam container, which is referred in the ensuing to as the 'shear stack'. The internal dimensions of the shear stack are 4.8 m (length) by 1 m (width) by 1.2 m (depth).[57]

The flexible shear stack was employed to mimic free-field boundary conditions and minimise the effect of physical boundaries on the dynamic response of the soil. A further precaution in preventing boundary effects was taken by placing the structural model sufficiently far from the physical boundary. It is commonly agreed that even for rigid-wall experimental containers, structures of interest placed at a distance of 1-1.5 times the height of the container are not significantly affected by edge effects.[58] The IAB model was placed in the middle third of the shear stack's length (Figure 2).

3.3 | Soil properties

The physical properties of dry Leighton Buzzard sand[59,60] employed for the foundation and the backfill are shown in Table 1. The minimum and maximum density values for the sand were determined at 14.5 kN/m^3 and 16.2 kN/m^3 at the

TABLE 1 Foundation and backfill void ratio e [ ] and relative density D_r [%], reported in parenthesis, for dry Leighton Buzzard sand fraction B; specific gravity of soil grains = 2.65

Soil layer	Minimum	Maximum	Achieved
Foundation	0.635 (0)	0.827 (100)	0.687 (73)
Backfill	0.635 (0)	0.827 (100)	0.766 (32)

TABLE 2 Details of the five shaking table test configurations: NoEPS, EPS1, EPS2 have 0, 1 and 2 layers of PU foam, respectively; noCP, CP have released and connected pile heads

Test number	Designation	*PU* foam layers	Pile head fixity
1	*EPS2-CP*	2	Fixed
2	*EPS1-CP*	1	Fixed
3	*noEPS-CP*	0	Fixed
4	*noEPS-noCP*	0	Non-fixed
5	*EPS1-noCP*	1	Non-fixed

Technical University of Kaiserslautern in accordance with International Organization for Standardization.[61] The sand was pluviated in the shear stack following the procedure described in Kloukinas et al.[60] Ensuing the pluviation of a 400 mm-thick foundation layer to embed the piles, the sand was levelled in 5 mm-thick layers and densified by applying a white noise signal. Following the alignment of the IAB structure with the pile heads, the backfilling of the 600 mm tall abutments was completed. A density difference was achieved to mimic the stiffness contrast between the backfill ($\gamma = 15.0$ kN/m^3, $D_r = 32\%$) and the natural foundation soil ($\gamma = 15.7$ kN/m^3, $D_r = 73\%$), by not levelling the sand but simply applying white noise at the end of pluviation. The corresponding 'effective' low-strain shear wave propagation velocities, at 2/3 of the thickness of the backfill and the foundation soil layers, were estimated by means of the Hardin and Drnevich equation[62] at 105 m/s ($G = 17$ MPa) and 133 m/s ($G = 28$ MPa), respectively.

3.4 | CI: Polyurethane foam

Some test configurations made use of polyurethane (*PU*) sheets placed behind the abutment wall. This type of foam was employed to reproduce the EPS geofoam used in real integral bridge applications. PU foam was selected for the tests as it is generally softer than the EPS geofoam which facilitates the scaling process (section 4). Furthermore, PU foams are easy to use and store in the laboratory. The density of the CI used in this study was 16 kg/m^3.

A series of loading tests were performed to determine the elastic modulus E_i of the CI using an oedometer cell equipped with an Linear Voltage Differential Transducer (LVDT) sensor to measure displacement. Circular foam samples with a diameter of 75 mm and a thickness of 30 mm were cut and placed inside the oedometer to be tested at three different stress levels: 7.5, 15 and 21 kPa. The initial overburden pressure was set at 5 kPa as to reproduce the static stress on the foam elements installed behind the abutment wall. The displacement data were acquired at a sampling rate of 1 Hz. Notwithstanding the uncertainty in the measurements due to the high compressibility of the foam, valuable data were obtained which can be used in numerical simulations. Based on laboratory testing, E_i could be evaluated from correlations available in literature, as a function of foam density (ρ_i), confining stress (σ_3) and loading rate.[31,63–65] A value of E_i ranging between 3.6 and 6.3 kPa was found for the PU. Similar relationships, available in literature for EPS geofoam, provide the Young's modulus, E_i in the range 4.5-10 kPa for $\rho_i = 20$ kg/m^3.[66]

3.5 | Test configurations

Given the general objectives of the test programme, five (5) test configurations were investigated, combining different PU foam thickness values with different pile-to-abutment connections, i.e., connected (CP) vs disconnected (noCP). Details of the test configurations are shown in Table 2. After completion of each test and before proceeding to the next model configuration, the soil behind the abutment wall was excavated so that the rest of backfill remained at the angle of repose (Figure 3). The amount of soil replaced was limited by the need to avoid repositioning of accelerometers in the backfill - notably

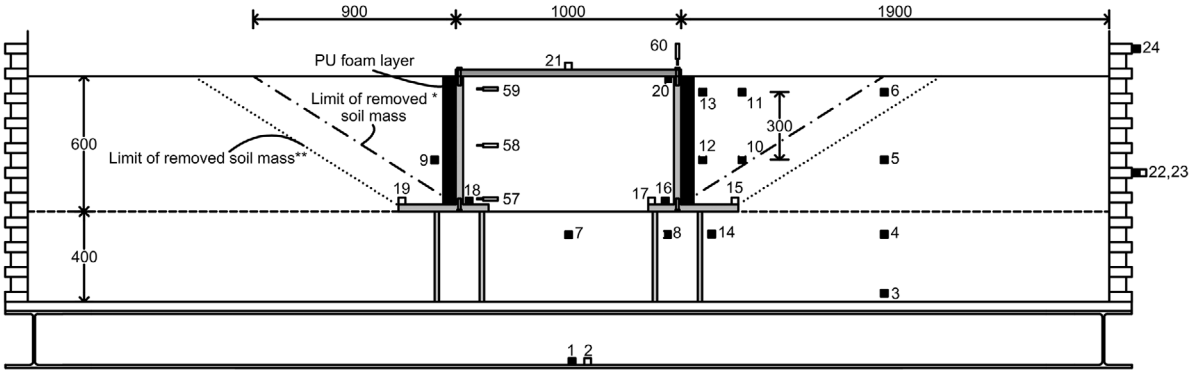

FIGURE 3 Layout of the instrumentation placed in the soil container and sensor numbering used in section 5 for presentation of results. All dimensions in mm. Right side of the soil container is West. The dotted-dashed line represents the limit of soil mass removed between test configurations 1-2, 2-3 and 4-5, indicated as *. The dotted line represents the limit of soil mass removed between test configurations 3-4, indicated as **. In this latter case, pile heads needed to be set up for the 'noCP' configuration (Table 2)

accelerometer #6 near the soil surface. Only when switching from configuration 3 to 4 (i.e., NoEPS-CP, NoEPS-noCP) as per Table 2, a larger amount of soil was removed, and accelerometer #6 was repositioned. In that case, the soil removed more-or-less corresponds to a hypothetical failure wedge originating from the edge of the footing. This approach was considered acceptable since soil response was within a linear/equivalent-linear regime, away from failure.

The pile head connectors and PU foam were then re-arranged, and the backfill was reinstalled. The test sequence was designed to optimise the preparation of each configuration.

4 | PHYSICAL MODEL DEVELOPMENT

The design of the model was governed by the capabilities of the testing equipment and was aimed at addressing key SSI aspects of the response under seismic excitation. Following an overview of the relevant scaling laws, the model was designed at a reasonable size to be capable of capturing the salient SSI effects. Once the model was defined, the layout of the instrumentation was designed and the seismic input was selected, as explained in the following.

From a design point of view, the proper physical modelling of SSI allows numerical simulations of the tests providing useful data for structural engineering modelling and integrating the current procedures suggested for static cases in the appendix of PD 6694-1.[26]

4.1 | Dimensionless parameters influencing SSI and scaling laws

For the definition of a suitable physical model, a fundamental dimensionless parameter to be preserved is the soil-to-wall relative flexibility (d_w) as defined by Veletsos and Younan,[67] Equation 1. In this expression, G_S is the shear modulus of the backfill, H_W is the height of the abutment wall and D_W is the flexural rigidity per unit wall width under plane strain conditions, given by Equation 2

$$d_W = G_S \ H_W^3 / D_W \tag{1}$$

$$D_W = E_W \ t_W^3 / \left[12\left(1-\nu_W^2\right)\right] \tag{2}$$

in which E_W, t_W and ν_W are the elastic modulus, the thickness and the Poisson's ratio of the abutment wall, respectively. A retaining wall can be considered rigid if $d_w < 1$ and flexible if $d_w > 5$.[68]

An associated parameter is the relative flexibility between the rotational constraint atop the abutment and the retained soil, (d_θ), which can be defined according to Veletsos and Younan[67] as

$$d_\theta = G_S \ H_W^2 / K_d \tag{3}$$

where K_d is the rotational flexural rigidity of the bridge deck per unit deck width. In the same vein, a wall is considered rotationally sensitive if $d_\theta > 1$ and firm if $d_\theta = 0$. An issue to be addressed when designing the physical model is the connection between the deck and the wall, and how stiffness variations between the two components influence the behaviour. Considering a symmetric model (e.g., a simple portal configuration), the stiffness K_d can be represented by a rotational spring whose modulus ranges between $K_d = 8\, E_d\, I_d/L_d$ (perfect fixity at mid-span) and $6\, E_d\, I_d/L_d$ (perfect pin at mid-span), where E_d is the deck elastic modulus, I_d the deck moment of inertia ($= t_d^3/12$) and L_d the deck length. An analogous equation can be defined for the relative flexibility between the rotational constraint at the base of the abutment and the soil.[67]

In the presence of a CI such as a PU foam placed between the abutment wall and the soil, an extension to the model introduced by Veletsos and Younan[67] was proposed by Horvath[69] and is expressed by Equation 4

$$d_i = 2\, G_S\, t_i/(E_i\, H_W) \tag{4}$$

where t_i and E_i are the thickness and elastic modulus of the CI layer, with the rest of parameters defined above. An analytical elastodynamic solution for the earthquake thrust on retaining walls enhanced by a geofoam layer has been developed by Mylonakis et al,[33,34] which reproduces available numerical results.[70]

The scale factor for the abutment wall can be obtained by matching the relative flexibilities in Equation 1 for the model, M, and the prototype, P, that is $(d_w)_{,M} = (d_w)_{,P}$. Introducing the geometric scale factor $\lambda = (H_W)_{,P}/(H_W)_{,M}$, the scaling factor for the elastic moduli of the wall material $\lambda_E = (E_W)_{,P}/(E_W)_{,M}$ and the scaling factor for the soil shear moduli $\lambda_G = (G_S)_{,P}/(G_S)_{,M}$, it is straightforward to show that the ratio of wall thicknesses between model and prototype is

$$\frac{t_{w,M}}{t_{w,P}} = \left(\frac{1}{\lambda}\right)\left[\left(\frac{1-\nu_{w,M}^2}{1-\nu_{w,P}^2}\right)\frac{\lambda_E}{\lambda_G}\right]^{1/3} \tag{5}$$

In the same vein, introducing the scaling factor for the deck length $\lambda_d = L_{d,P}/L_{d,M}$ and the scaling factor for the elastic moduli of the deck material $\lambda_{Ed} = (E_d)_{,P}/(E_d)_{,M}$, and repeating the above exercise using Equation 3 yields the ratio of deck thicknesses between model and prototype

$$\frac{t_{d,M}}{t_{d,P}} = \left(\frac{1}{\lambda^2 \cdot \lambda_d}\right)^{1/3}\left[\frac{\lambda_{Ed}}{\lambda_G}\right]^{1/3} \tag{6}$$

in which the plane strain assumption has not been adopted as the deck is not transversely constrained. Note that if one employs identical geometric scaling factors for the wall height and the deck length (i.e., if $\lambda = \lambda_L$), same materials for the deck and the wall (i.e., $\lambda_E = \lambda_{Ed}$) and neglects the (usually small) effect of Poisson's ratio mismatch between model and prototype, Equation 6 reduces to Equation 5.

With reference to the CIs, introducing the scaling factor for the elastic moduli of the inclusions $\lambda_i = (E_i)_{,P}/(E_i)_{,M}$, the ratio of the inclusion thicknesses between model and prototype is obtained from Equation 4 as

$$\frac{t_{i,M}}{t_{i,P}} = \left(\frac{1}{\lambda}\right)\left[\left(\frac{1-\nu_{i,M}^2}{1-\nu_{i,P}^2}\right)\frac{\lambda_i}{\lambda_G}\right]^{-1} \tag{7}$$

Wave propagation in the soil can be described in terms of the familiar dimensionless wavenumber

$$k = \omega\, H/V_S \tag{8}$$

where ω is the cyclic frequency of the shear wave, H is the thickness of the soil layer and Vs is the shear wave propagation velocity in the soil.

Introducing the scaling factor for shear wave propagation velocity $\lambda_V = V_{S,P}/V_{S,M}$, one obtains the ratio of excitation frequencies between model and prototype in the form

$$\left(\frac{\omega_M}{\omega_P}\right) = \lambda/\lambda_V \tag{9}$$

The above scaling factor can be further explored by recalling that λ_V is proportional to ${\lambda_G}^{1/2}$ while λ_G for non-cemented sands is approximately equal to $\lambda^{1/2}$.[71–73] This yields the simpler expression

$$\left(\frac{\omega_M}{\omega_P}\right) \approx \lambda/\lambda^{1/4} = \lambda^{3/4} \tag{10}$$

which can be interpreted as a dynamic time scaling factor, λ_t (section 4.4) in accord with the geotechnical literature71-73. It is noted that the alternative expression $(\omega_M/\omega_P) = \lambda^{1/2}$ recommended in the structural engineering literature[74] should not be used in problems of this type as it does account for the dependence of soil shear modulus on overburden pressure.

For the IAB at hand, considering an abutment wall with prototype height $H_{W,P} = 6$ m and model height $H_{W,M} = 0.57$ m (Figure 2), yields a geometric scale factor $\lambda \approx 10$. Using $G_{S,M} \approx 17$ MPa and $G_{S,P} \approx 40$ MPa corresponding, respectively, to an average value for loose Leighton Buzzard laboratory sand along the height of the wall[59] and a medium dense prototype backfill, yields a shear modulus scaling factor $\lambda_G \approx 2.4$. Using $E_{W,M} = 69$ GPa for the elastic modulus of an aluminium model (section 4.2) and $E_{W,P} \approx 30$ GPa for the concrete prototype, yields $\lambda_E \approx 0.4$. Ignoring the mismatch in Poisson's ratios between model and prototype, Equation 5 yields $t_{W,P} = 0.032\ \text{m} \times 10 \times (2.4/0.4)^{1/3} \approx 0.60$ m.

Likewise, considering a prototype span of 30 m corresponding to a deck length scaling factor $\lambda_d = 30$, Equation 6 yields the prototype deck height $t_{d,P} = 0.03\ \text{m} \times (10^2 \times 30 \times 2.4/0.4)^{1/3} \approx 0.80$ m where the Poisson's ratios mismatch has, again, been ignored (section 4.2). The CI can also be scaled up to prototype dimensions using Equation 7 to $t_{ci,P} = 0.03\ \text{m} \times 10 \times (1.4/2.4) \approx 0.20$ m. In this calculation, $(E_i)_{,P} \approx 7$ kPa, $(E_i)_{,M} \approx 5$ kPa were assumed leading to $\lambda_i = 1.4$.

Based on the above values, Equations 1, 3 and 4 yield $d_w \approx 15$, $d_\theta \approx 5$ and $d_i \approx 300$, respectively. Also, frequency scaling (i.e., dynamic time) can be readily obtained from Equation 10 as $(\omega_M/\omega_P) = 10^{3/4} \approx 5$.

The following are worthy of note: (a) The results obtained for the deck thickness can be extended to multiple-span bridges considering the zero-moment location. For example, for a two-span bridge if the pier constraint is considered as a hinge, the bending moment for horizontal loads is equal to the single-span case. For different constraints, multiple-span bridges and considering the effect of vertical loads, case-specific scaling laws would be needed. (b) The values of $d_{w,}$ d_θ and d_i correspond to a relatively flexible abutment, which is suitable for capturing the relevant interaction phenomena. (c) Generic scaling laws, such as those available in literature, might be inapplicable to special problems involving SSI like the one at hand. Evidently, the scaling laws developed in this section complement and extend the state-of-the-art in the area.[71–73,75]

With reference to soil strength, it is fair to acknowledge that for conditions close to peak strength, strong dilatancy effects, due to low levels of overburden stresses, will naturally lead to increased strength. However, such conditions do not arise in the tests at hand (e.g. the safety factors against passive earth pressures on the abutment walls typically exceed 10) and, therefore, the linear/equivalent linear scaling procedures outlined above are sufficient.

4.2 | Design of integral bridge model

The model geometry adopted in the tests and displayed in Figure 3 accommodates the constraints given by the dimensions of the shear stack and the maximum payload of the shaking table. The established maximum soil height was 1 m, the foundation soil tickness was 0.4 m (equal to the footing width B), and the backfill soil height was 0.6 m (equal to the abutment wall height H). As already mentioned, in the absence of thermal effects, two different scaling factors for the deck and the abutment walls were employed to allow the bridge deck fit in the soil box. The soil behind the abutment at each side of the box was about three times the height of the abutment wall, dimension that is considered sufficient to avoid boundary interaction effects with the shear stack wall and to ensure free field conditions. The abutment wall and the wall footing were made of 5083 type aluminium alloy plates ($\gamma_{al} = 27$ kN/m^3, $E_{al} = 69$ GPa,$\nu_{al} = 0.3$).

To inspect, access and operate in the internal space between the abutment walls during the experimental campaing, the deck comprises four steel beams ($\gamma_{st} = 80$ kN/m^3, $E_{st} = 210$ GPa, $\nu_{st} = 0.3$) having length of 1 m, width of 0.1 m each and tickness of 0.03 m. For the pile foundation, 16 hollow tubes made of 6063 type aluminium with outer diameter $d_p = 22$ mm and thickness $t_p = 1.2$ mm, equally spaced at a distance of 300 mm, were employed. To allow for rotation of the pile cap, the pile tips were not in contact with the base of the container. Instead, the pile tips were inserted into a plug realised by superposing two 15 mm-thick plywood layers, perforated at the locations of the eight piles. At the base of each plug, a disk-shaped layer of PU foam with a 3 mm thick nylon disk on the top was placed to allow for vertical movement (Figure 4A). The soil in the first 400 mm of the box was pluviated in layers and levelled at each layer having the instrumented piles in

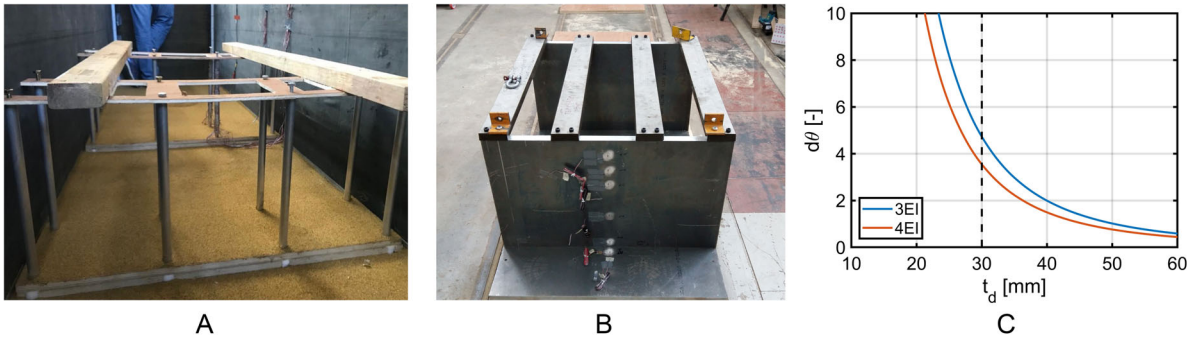

FIGURE 4 A, IAB model tested, B, relationship between d_θ (Equation 4) and deck thickness (t_d)

position as shown in Figure 4A. To protect the instrumentation, the piles were not driven, but instead they were installed in the box first, and the soil was pluviated around them. While this approach does not model installation effects (which is not the focus of this research), it is common practice in such tests, as it does not affect the main phenomena explored and allows for better control of the near-pile soil properties.[76,77]

The bolted connection between (a) the abutment walls and the footings (12 bolts per side), and (b) the abutment walls and the deck (two bolts on each side of a beam, for a total of eights bolts per side) was made with M12 steel bolts (Figure 4B). The stiffness of the deck-abutment connection was checked by means of a static load test performed on the bridge prototype, confirming that the stiffness was close to that of a fixed constraint. The connection between each pile and the footing was made by hammering a 30 mm thick nylon hollow-cylindric plug provided with a M12 thread, inside the aluminium tube. Then, a riveted steel stud was inserted in the plug through a hole in the footing. In doing so, it was possible to manufacture two configurations for the pile: (a) pile fixed to the footing (CP condition), made by fixing the stud with a nut (female screw); (b) pile non-fixed (i.e., free to rotate) at the top by removing the nut.

To measure strains with strain gauges placed along the two faces of the wall, the wall should be sufficiently flexible, a condition attained for $d_W > 5$ (section 4.1). Considering $d_W = 15$, in line with other related studies[60], a wall thickness $t_W = 32$ mm was established by means of Equation 1 using, as a first approximation, $G_S \approx 15$ MPa, $E_W = 69000$ MN/m^2, $H_w = 0.6$ m, and $\nu_W = 0.3$. Based on the hypothesis that the strain gauges work at their minimum operational level ($\varepsilon_a \approx 10^{-5}$), the minimum wall bending moment M_d required to trigger the instrumentation is estimated at 125 Nm. Based on this value and using the strength-of-materials equation

$$\varepsilon_a = \mathrm{M_d} \cdot t_w/(2 \cdot D_W) \tag{11}$$

in conjunction with elementary Mononobe-Okabe theory,[62] the minimum peak ground acceleration on the shaking table required to trigger strain measurements is back-calculated at around 0.1 g.

A plot of d_θ as a function of deck thickness t_d is displayed in Figure 4C. It can be observed that the parameter tends to infinity for $t_d \leq 20$ mm (flexible deck), to zero for $t_d \geq 60$ mm and attains values between 0 and 10 for $20 \leq t_d \leq 60$ mm. In order to reproduce the relative flexibility between deck and abutment in the prototype IAB, a nominal deck thickness $t_d = 30$ mm was adopted in the model.

4.3 | Instrumentation layout

The instrumentation employed consists of accelerometers, strain gauges and LVDTs. The total number of channels available for the tests was 64. A total of 24 accelerometers (18 horizontal and six vertical) were installed. As depicted in Figures 3 and 4, accelerometers (two horizontal and two vertical) were mounted at the base of the shaking table and on the external wall of the shear stack. Since the model is symmetric, only one side (right side in Figure 3) of the shear stack is fully instrumented, with five horizontal accelerometers placed in the foundation soil, six horizontal accelerometers in the backfill, with concentration in the area in front of the abutment wall and the free field, and around piles. Finally, seven accelerometers were mounted on the bridge model to control the structural response and particularly the rocking of the footing, by means of two vertical sensors placed at the end sections of the footing (i.e., 15 and 17). Strain gauges were placed on the bridge model to monitor wall and pile bending: 10 on the central section of the wall and four on the footing, while other 18

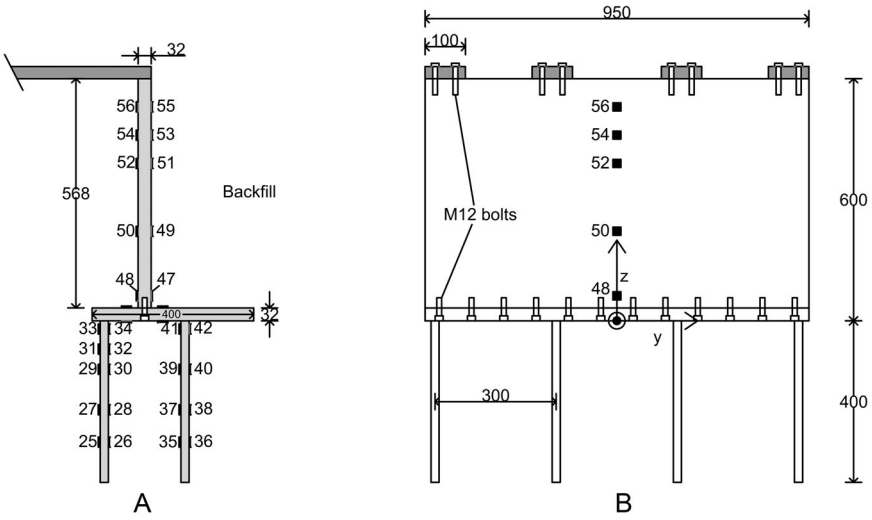

FIGURE 5 Layout of the strain gauges on the model (A) longitudinal view, (B) transversal view (channel numbering used in section 5 for results presentation)

TABLE 3 List of selected accelerograms and associated information including record ID used in the tests, station code and component considered (comp.) NS = North-South, EO = East-West, Z = vertical

ID	Date (DD/MM/YY)	Station	$V_{S,30}$ (m/s)	M_w	R (km)	Comp.	PGA (g)	T_R (years)
1	18/01/2017	AMT	670	5.4	14.4	NS	0.12	50
2	26/10/2016	CSC	698	5.4	20.2	NS	0.08	50
3	21/03/1998	SELE	519	5	10	EO	0.14	50
4	30/10/2016	CSC	698	6.5	15	NS	0.16	100
5	24/08/2016	AMT	670	6.2	8.5	NS	0.53	500
6	30/10/2016	AMT	670	6.5	26.4	EO	0.4	500
7	18/01/2017	AMT	670	5.4	14.4	Z	0.06	50
12	30/10/2016	AMT	670	6.5	26.4	Z	0.32	500

were put on two instrumented piles, as displayed in Figure 5. Finally, three horizontal and one vertical LVDTs were placed on the wall to measure the corresponding transient and permanent displacement. The disposition of the strain gauges is illustrated in Figures 5A and 5B where a longitudinal and transversal view of the IAB model is shown.

4.4 | Selection, scaling and testing sequence of strong motion records

Strong ground motion records were selected using the Italian Accelerometric Network (RAN). The records are openly accessible on the European Strong Motion Database website,[78] (www.esm.mi.ingv.it). The 5% damped elastic reference spectra according to the Italian code[79] were defined for L'Aquila (Italy), characterised by medium to strong seismicity, using three different reference return periods (T_R) of 50, 100 and 500 years. A total of six horizontal and two vertical ground motion were chosen - mostly from the records of the 2016 Central Italy earthquakes,[80,81] with moment magnitude (M_W) ranging from 5 to 6.5 and epicentral distance (R) between 8 and 27 km. A soil B class was assigned based on V_S profiles (obtained with down-hole or cross-hole tests) to all the selected seismic stations, which are located in the Italian municipalities of Amatrice (AMT), Cascia (CSC) and Sellano (SELE).

The complete list of selected ground motions is reported in Table 3. The spectra of the natural records were first compared with the elastic reference spectra for L'Aquila at different T_R's to verify a rough spectrum compatibility. Then, an equivalent linear analysis was performed using the code DEEPSOIL[82] to deconvolve the selected records through the soil to establish the 'bedrock motion'.[78] This was done considering an initial damping ratio of 2% in softer layers and 0.5% in harder layers[83] and using the Seed and Idriss 1991 shear modulus reduction and material damping curves for sand as per DEEPSOIL option.[84] Figure 6A depicts the acceleration response spectra of the deconvolved input motions used in the experimental tests, in the unscaled (solid lines) and scaled (dashed line) case, respectively.

Subsequently and according to the relationships developed in section 4.1, all original records were scaled (compressed) in time by applying a scale factor $\lambda_t = 5$. The effect of time scaling is evident in Figure 6B by comparing the Fourier

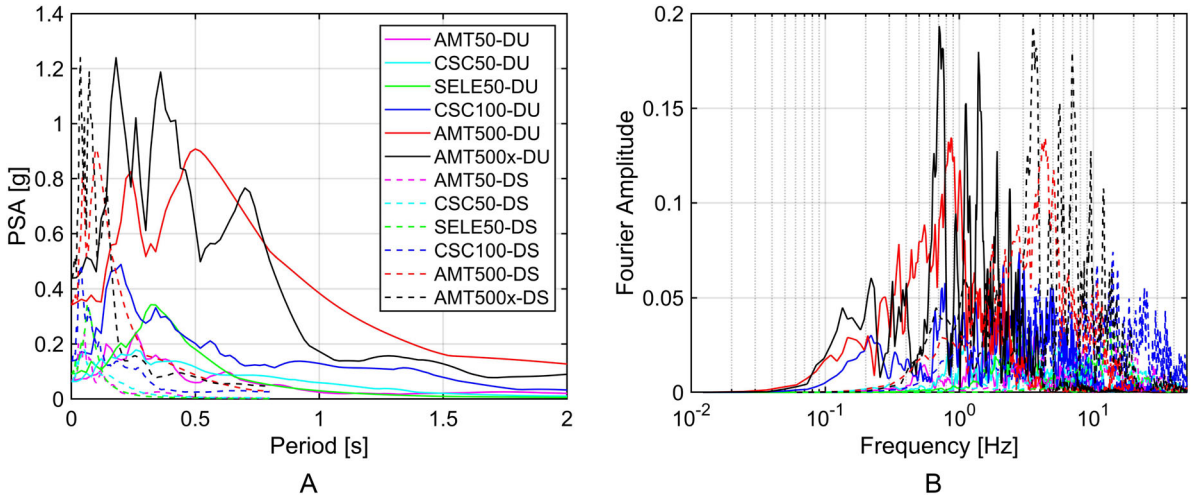

FIGURE 6 A, Pseudo-spectral acceleration (PSA) response spectra of the deconvolved unscaled (DU) versus deconvolved scaled (DS) earthquake records by a time factor $\lambda_t = 5$; B, fast Fourier transform of earthquake records DU and DS

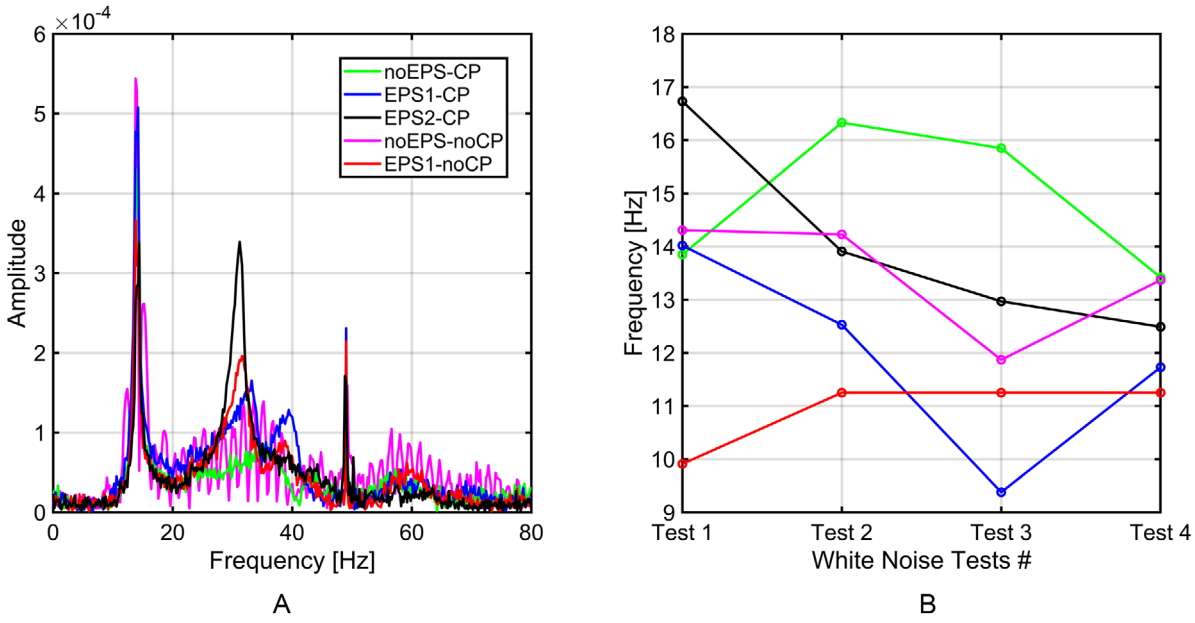

FIGURE 7 A, Frequency response for *EPS2-CP* in hammer tests, B, evolution of resonant frequency of all configurations determined through white noise tests *W1*, *W2*, *W3* and *W4* as recorded by accelerometer 22

amplitude spectra. For a few cases, a time scale factor of 1 was adopted in order to excite lower frequencies. Accordingly, the resulting sample frequencies are $f = 200$ Hz for $\lambda_t = 1$ and $f = 1000$ Hz for $\lambda_t = 5$. In the selection process, attention was paid to frequency content by excluding time-scaled records ($\lambda_t = 5$) whose frequency content was close to the natural frequencies of the shear-stack (Figure 7).[57,85]

For each of the test configurations reported in Table 1, the shear stack was excited by the selected strong motions in the order outlined in Table 4, beginning with the five records at 1000 Hz sampling frequency ($\lambda_t = 5$) with increasing return period. At the end of these tests, Record 6 (i.e., the deconvoluted signal for the 30/10/2016 AMT recording) was applied with a sampling frequency of 200 Hz (*S10* in Table 4). For configuration *EPS1-noCP* (disconnected pile heads and one layer of EPS), an additional excitation step (*S10*) involving Record 6 (horizontal) and Record 12 (vertical) was applied at a sampling frequency of 200 Hz to investigate the influence of vertical excitation on the response. The intermediate exploratory white noise tests (steps *Wi*) listed in Table 4 were applied at the end of each suite of records corresponding to a specific T_R group (Table 3), to investigate the dynamic properties of the system at specific milestones. Such white noise shakings were also employed before application of shaking to all new configurations (i.e., W1 in Table 4). This aimed at

TABLE 4 Summary of the excitation sequence for each test configuration: H = horizontal motion V = vertical motion, SM = soil surface measurement. Sampling frequency of 1000 Hz refers to records scaled by $\lambda_t = 5$

Step no.	Input motion (*IDs* from Table 3)*	SM	Direction	Sampling frequency (Hz)
W1	White noise	Yes	H	–
S1	Record 1	No	H	1000
S2	Records 1 + 7	No	H + V	1000
S3	Record 2	No	H	1000
S4	Record 3	Yes	H	1000
W2	White noise	Yes	H	–
S5	Record 4	Yes	H	1000
W3	White noise	Yes	H	–
S6	Record 5	Yes	H	1000
S7	Record 6	Yes	H	1000
S8	Records 6 + 12	Yes	H + V	1000
W4	White noise	Yes	H	–
S9	Record 6	Yes	H	200
*S10***	Records 6 + 12	Yes	H + V	200

*After deconvolution.

**Used only in the last testing configuration (*EPS1-noCP*).

achieving a preliminary densification after soil replacement and set up of a new model configuration (Figure 3). The white noise signals had a bandwidth of 1-100 Hz and a root mean square value of acceleration equal to 0.005 g. Horizontal and vertical hammer tests were also carried out before step *W1* and a horizontal one after step *W4*. Laser pointers and manual measurements were taken at fixed grid points to assess soil surface deformations. Such surface measurements were taken after each step for records associated with $T_R = 100$ years and $T_R = 500$ years, while for records of $T_R = 50$ years the measurements were made only at the end (following step *S4*) as indicated in column *SM* in Table 4.

5 | TEST RESULTS AND DISCUSSION

The tests results are reviewed to investigate, for each configuration and with increasing shaking intensity: (a) the natural frequencies of the system (section 5.1), (b) the various acceleration responses and the free-field amplification (section 5.2); (c) the displacement response of the abutment (section 5.3); (d) the bending strains in the abutment and the piles (section 5.4) and (e) the backfill settlement (section 5.5), aimed at capturing the nonlinear behaviour of soil and comparing the different mitigation measures.

5.1 | Natural frequency measurements (white noise - hammer test)

The resonant frequency of the model was investigated before, in-between, and after the input motions were applied. Two major techniques, namely hammer and white noise, were used to this end. Hammer testing was conducted by impacting the model structure with a piezo-electric load cell instrumented hammer. The resonant frequencies of the system were identified by evaluating the transfer function between the input and output signals. A similar procedure was employed for the white noise testing where the system was excited using the shaking table. In both hammer and white noise tests, the response was investigated by processing horizontal acceleration readings.

Figure 7 illustrates the evolution of the resonant frequencies of the system throughout the experimental campaign. Since typical IABs do not involve CIs and released pile heads, the *noEPS-CP* configuration was assumed as the benchmark case. Prior to the application of seismic excitations, *noEPS-CP*, *noEPS-noCP*, and *EPS1-CP* systems all exhibited a fundamental natural frequency around 14 Hz.

Upon application of excitation, an increase in natural frequency would be anticipated due to soil densification. This trend was not manifested in tests with CIs (e.g. *EPS2-CP* in Figure 7B), possibly due to rearrangement of soil particles.

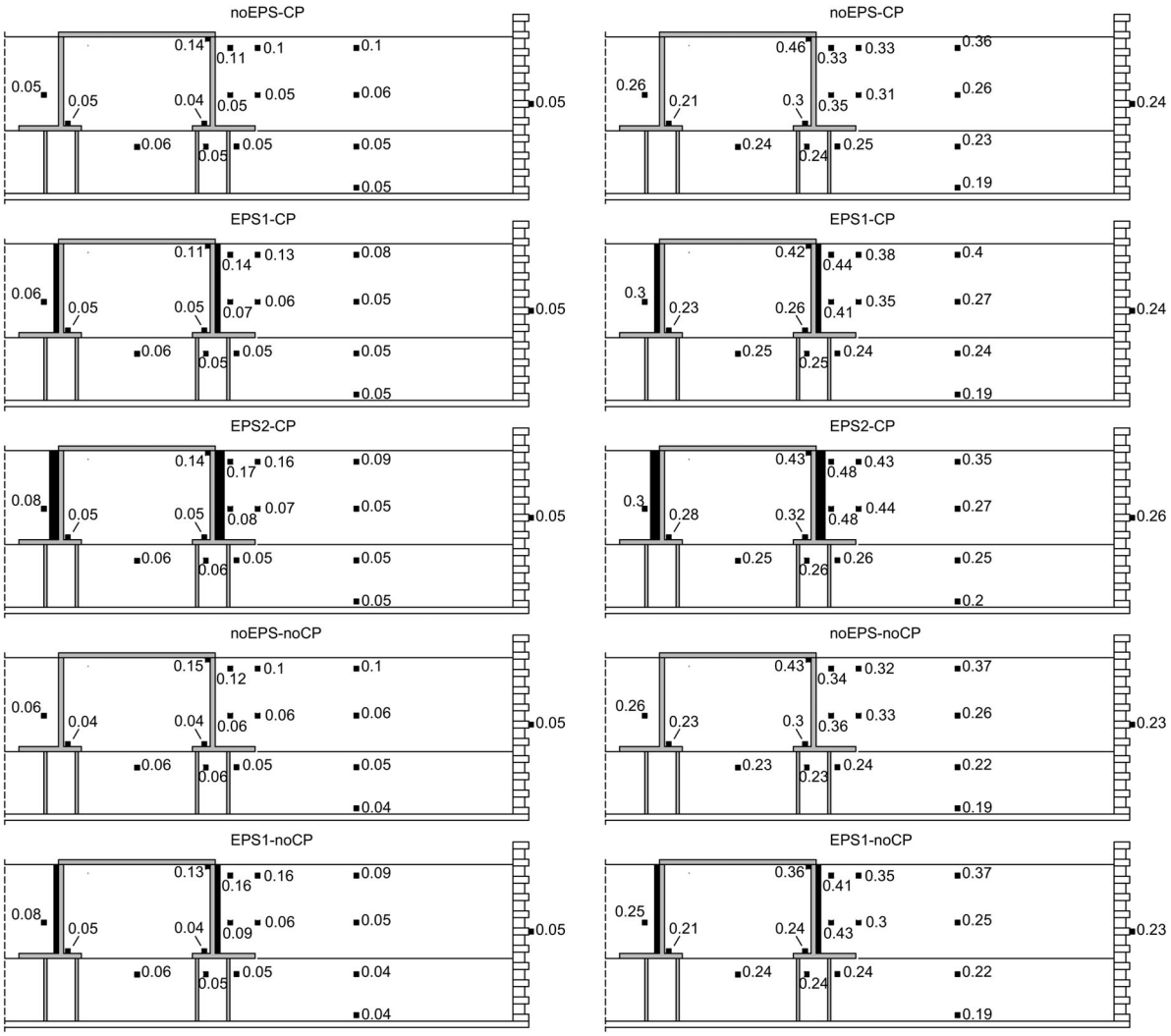

FIGURE 8 Box with maxima values of acceleration in *g* for tests *S1* (left) and *S7* (right) (Table 4). Right side of the soil container is West

When the shaking was increased (i.e., *W3* to *W4*), no clear trend was obtained. This might be attributed to some dislocations in the system.

5.2 | Acceleration response

The analysis of the results in terms of acceleration response histories indicates that CIs decrease accelerations at the abutment wall and increase those in the backfill. The thicker is the CI, the more pronounced is the trend. Connections at the pile heads have only minor influence on these accelerations. Figure 8 depicts the maximum accelerations recorded by the accelerometers for all configurations, for tests *S1* and *S7*. Similar trends were observed for 'weak' (*S1*) and 'strong' (*S7*) seismic excitations.

Evidently, the accelerations for *S7* (right column in Figure 8) in the free field array (accelerometers 3, 4, 5, 6 as per Figure 3) attain the same value at the bottom of the soil container (about 0.2 g) regardless of the test layout. The free-field array shows amplification along the soil column, and limited differences are observed between the different configurations especially for accelerometers 3 and 4. The recording at accelerometer 5 (free field) and 22 (West wall of the shear stack) are similar, thus confirming that the box is deforming together with the soil. The amplification effect in the free field can be observed by the value of acceleration in accelerometer 6, which is larger than the one recorded lower in the same soil column and reaching 0.35-0.4 g depending on the case. As expected, the free field acceleration is not affected by the modifications in the soil-structure system and confirms that boundary effects were avoided in the experimental set up.

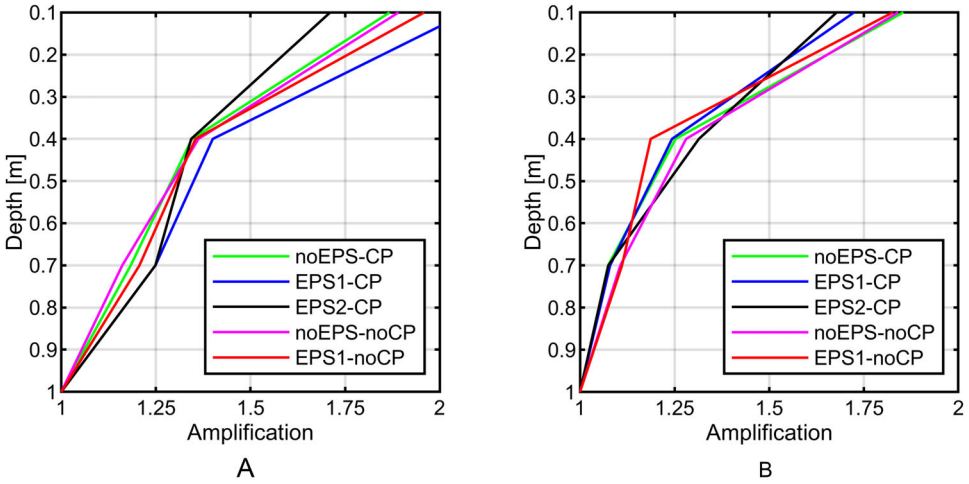

FIGURE 9 Maximum amplification ratio $a_{max}(z)/a_0$ in the free-field. A, *S7*, B, mean value for all input motions in each configuration

The effect of CIs can be investigated by comparing the results obtained with and without the PU foam. For example, for the *noEPS-CP* configuration, the free field acceleration is 0.26 g while the values of acceleration recorded by accelerometers 10 and 12 are 0.31 and 0.35 g, respectively. Accelerometers 11 and 13, which are close to the ground surface, recorded peak accelerations of 0.33 g and 0.35 g. The accelerations recorded in the backfill increase from *noEPS* to *EPS1* and *EPS2* cases. For accelerometer 13 the recording is 0.33, 0.44 and 0.48 g, respectively, confirming the trend highlighted for test *S7*. While in the case without CI the peak acceleration atop the bridge (i.e., accelerometer 20) was 0.46 g, it dropped to 0.42 g and 0.43 g with one layer and two layers of PU foam, respectively. This trend is confirmed by observations from parametric studies on integral abutments.[86] When the intensity is lower, as in test *S1* (Figure 8 left), and in the absence of EPS, the instruments located at 0.4 m depth recorded accelerations as high as those on the ground surface.

When the pile heads are disconnected from the footing, as in the *noEPS-noCP* case, peak accelerations for instruments 12 and 13 are 0.36 and 0.34 g, respectively, while the peak acceleration of the bridge is 0.43 g. Similarly to the case of piles connected to the footing, *noEPS-CP*, the addition of a CI causes an increase in backfill accelerations (0.43 and 0.41 g for accelerometers 12 and 13, respectively), while the acceleration on the bridge model is 0.36 g, which is the lowest observed on the *S7* test. This trend was not consistent in all tests (including *S1*), so it is not possible to confirm the beneficial effect of pile head releases on acceleration.

Figure 9A reports, for all configurations, the amplification factors evaluated in test *S7* for accelerometers 3, 4, 5, 6 (i.e., the free field array) by normalising acceleration responses with reference to the acceleration at the bottom of the container (accelerometer 3). Figure 9B presents the median values of the amplification factor for each configuration for all eight tests (different records). A similar trend in the median values is observed, with maximum amplification ranging from 1.68 to 1.85. The consistent level of amplification recorded by the free-field array amongst the different configurations highlights the minor effect of soil densification (soil in this location was not removed when preparing different experimental set-ups) during successive tests. This is also partly due to the high initial relative density of the physical model (Table 1).

Figure 10A shows the acceleration response history in *S7* test recorded by accelerometer 18 located on the West (right) footing close to the wall, for all five configurations. It can be observed that the acceleration slightly increases when adding the PU foam layers. For example, by comparing *noEPS-CP* (green plot) and *EPS2-CP* (black plot), the maximum absolute acceleration is 0.24 g in the first case and 0.31 g in second one. Disconnecting the pile heads from the cap (magenta and red plots) does not seem to have a considerable effect on accelerations.

It is worth noting that the levels of acceleration experienced by the bridge do not induce failure in the backfill (i.e., even for the case of 'strong' shaking *S7*); the margin of safety is at least 10 as computed based on available limit state solutions.[34]

5.3 | Displacement response

Displacement responses obtained with LVDTs show a reduction in displacements for the configurations with a CI. The reduction is higher for the cases with two layers of PU foam. Figure 11 presents the peak displacements recorded at the base and top sections of the abutment wall.

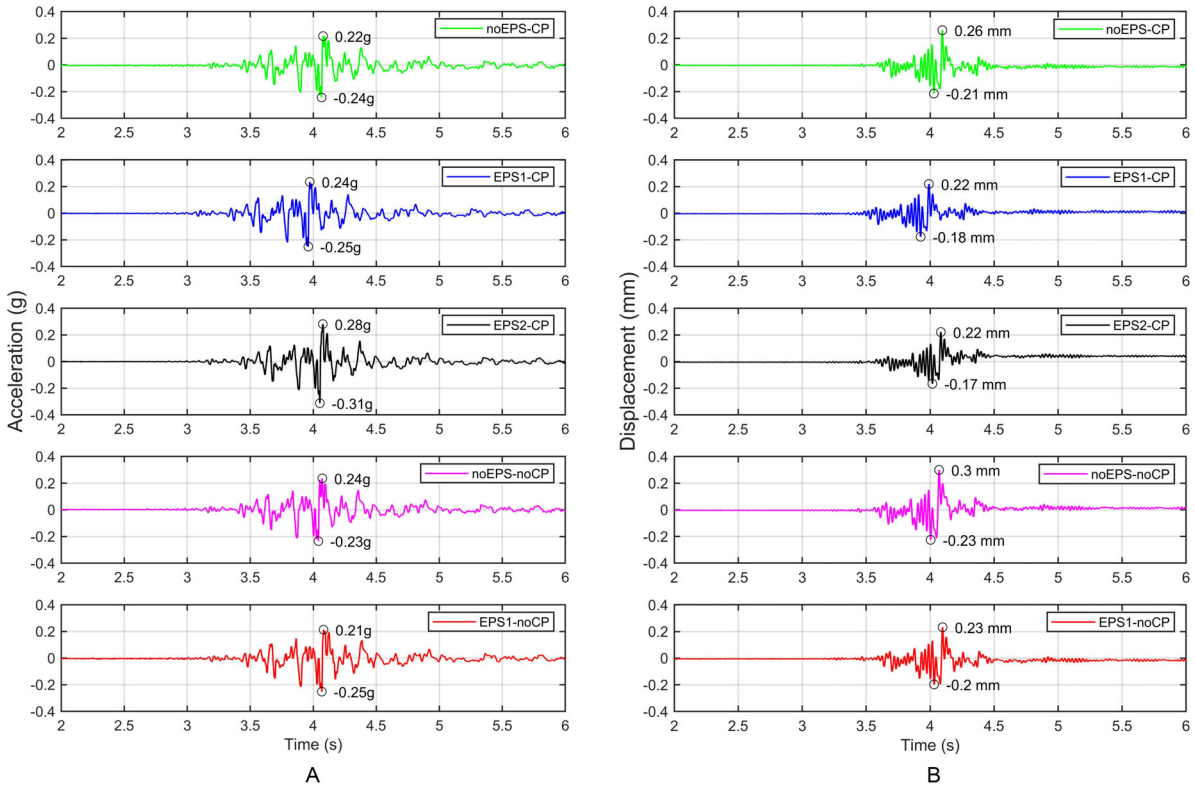

FIGURE 10 A, Time histories of horizontal acceleration recorded by accelerometer 18 (footing toe); B, time-histories of horizontal displacement recorded by LVDT, #57 in Figure 2, (abutment wall bottom) for each testing configuration and for shaking step *S7* as per Table 4

FIGURE 11 Peak displacements recorded at: A, abutment base; and b, abutment top for all configurations listed in Table 2 and each shaking step (*Si*) listed in Table 4

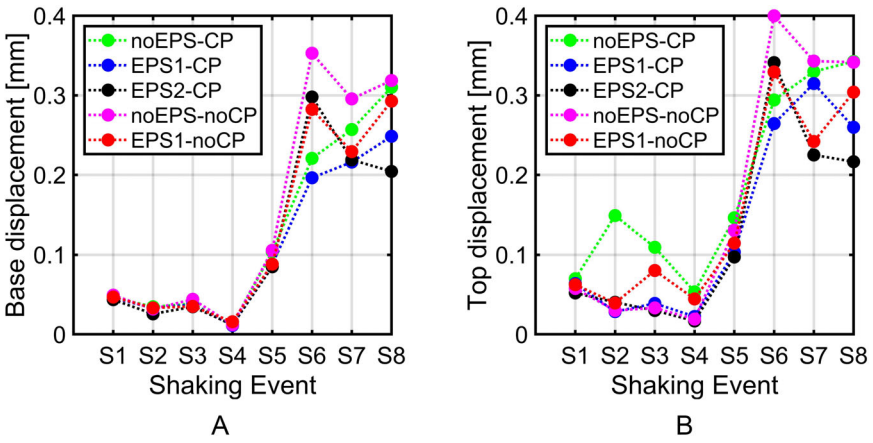

The responses presented in Figures 10 and 11 are quite similar. The trends are in all cases consistent, with the exception of *EPS1-noCP*. In this case the dispersion is also higher, and the difference relative to the other cases might be caused by some incidental variations of the load and the slight change in natural frequency of the system. In general, from a displacement viewpoint, there are no significant differences between the analysed cases, but some trends of the beneficial influence of EPS and noCP can be observed. LVDTs for bridge displacement monitoring were positioned on the East abutment wall, to avoid disturbing the strain gauges mounted on the West abutment. Figure 10B presents the displacements recorded by LVDT 57, which are located at the bottom of the East abutment wall. Such displacements have been also slightly influenced by the rocking of the wall foundation allowed in the set up. A preliminary assessment of foundation rocking carried out via double integration of the difference in vertical acceleration between accelerometers 15 and 17 showed that rocking rotation is of the same order of magnitude as the rotation of the wall evaluated by double integration of the vertical accelerations recorded by instruments 16 and 20, being about ~40% to ~ 60% of the rocking rotation of the footing for different configurations.

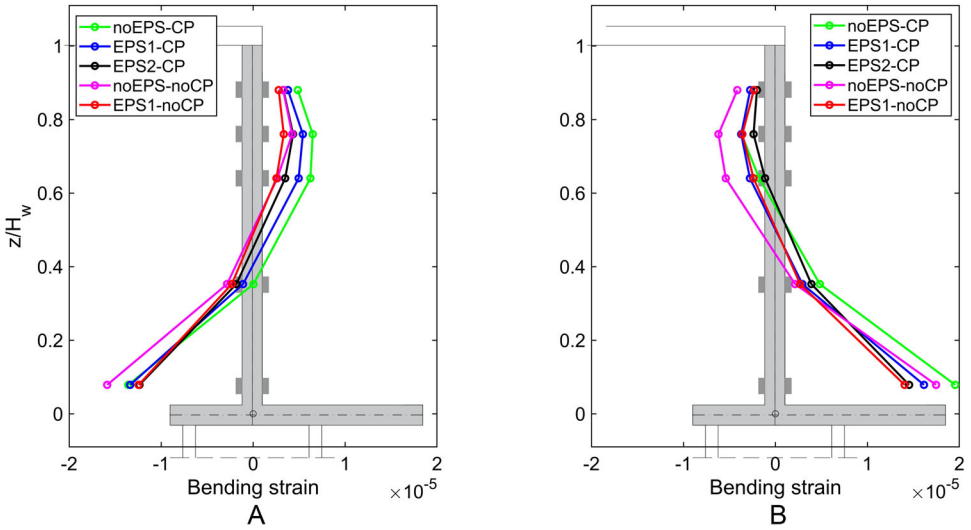

FIGURE 12 A, Maximum; and B, minimum bending strain on the abutment wall to *S7*

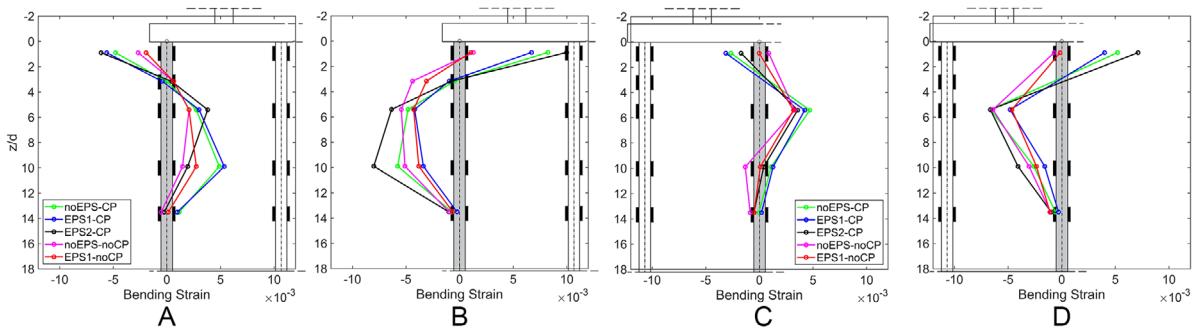

FIGURE 13 A, Maximum, and B, minimum pile bending strain on the East pile; C, maximum, and D, minimum pile bending strain on the West pile to *S7*

For the configurations involving pile heads connected to the footing, there is a reduction in terms of maximum displacement when passing from *noEPS-CP* configuration (0.26 mm) to *EPS1-CP* (0.22 mm). On the other hand, almost equal displacements are obtained for the *EPS2-CP* case. Disconnecting the pile heads from the footing leads to a slight increase in absolute maximum displacement that is 0.3 mm for *noEPS-noCP* and 0.23 mm for *EPS1-noCP*.

The *noEPS-CP* configuration with the highest recorded values of natural frequency after the *S4* shaking event exhibited the largest abutment wall top displacement, as depicted in Figure 11B.

Comparison of the displacements for configurations *EPS1-CP* and *EPS2-CP* suggests that the increased thickness of the CI may cause a softening effect around the abutment wall, where the structure is not adequately restrained by the backfill against lateral displacement. Indeed, the configuration with a single layer of CI, *EPS1-CP*, experiences lower levels of lateral translation under the action of the applied input motions. Similar findings are reported by Bathurst et al[45] where the insulation efficiency of the CI is given as a function of the wall height and the ratio of excitation-to-wall natural frequencies. As can be seen from Figure 7, *EPS1-CP* has the lowest natural frequency (about 9.5 Hz) in the third white noise test which was conducted immediately prior to *S6* excitation. Displacements are also affected by the different natural frequencies of the test configurations.[86] The above observations can be used in a comparative way to estimate the potential benefits in terms of displacement decrease for IABs when such mitigation measures are employed.

5.4 | Strain response

Strain gauge measurements along the stem of the wall (Figure 12) and the piles (Figure 13) confirm some of the anticipated trends as to the effectiveness of the mitigation strategies explored in the experimental campaign. Evidently, the presence of CI along the height of the wall leads to a reduction in bending strains, with the 60 mm thick layer of *PU* foam being more

effective than the 30 mm one. Pile head release alone is not sufficient to reduce wall bending, as the rotational stiffness of the footing is naturally governed by axial action in the two pile rows. On the other hand, when pile head release is employed in combination with PU foam, a higher bending reduction is achieved. The difference in shape between the two plots in Figure 12 can be attributed to the different response behaviour due to the active and passive resistance of the backfill under dynamic conditions. This complex behaviour is a key feature of IABs and has been investigated by some authors for the case of daily and seasonal cyclic motion due to thermal loading.[87,88] The topic of active and passive pressures in IABs needs further investigation in numerical studies for calibration of lateral pressure coefficients that can lead to more economical designs.

Figure 12 presents the variation of wall bending strain ε_w calculated from strain measurements on the abutment wall (strain gauges 47, 49, 51, 53, 55, Figure 5). The ε_w plots correspond to two different time instants, namely when the maximum (positive, i.e., tension of wall outer fibre - the one not in contact with the soil) and minimum (negative, i.e., compression of the same fibre) dynamic bending strains are attained. The strain response obtained in test *S7* is reported for all five configurations. Figure 12A shows the maximum dynamic strains. The maximum strain is naturally reached at the bottom of the wall: for *noEPS-CP* is $-1.36\bullet10^{-5}$, while, for EPS1-CP and EPS2-CP is -1.34 and $-1.24\bullet10^{-5}$, respectively. In the configurations, the piles were disconnected, the strain decreases from $-1.59\bullet10^{-5}$ to $-1.25\bullet10^{-5}$ for *noEPS-noCP* to *EPS1-noCP*, respectively. ε_w strains are zero at about half of the abutment height. In the upper portion of the wall, the maximum value is reached in configuration *noEPS-CP*, with a value of $4.85\bullet10^{-6}$. Figure 12B presents the minimum strain ε_w diagrams. At the bottom of the wall (strain gauge 48), ε_w for the case with connected piles are 1.95, 1.61 and $1.45\bullet10^{-5}$ for *noEPS-CP*, *EPS1-CP* and *EPS2-CP*, respectively. In the disconnected case, the minima are 1.75 and $1.4\bullet10^{-5}$ for *noEPS-noCP* and *EPS1-noCP*, respectively. The shapes of strain distributions match those in recent comparative numerical studies available in literature, even if there is a lack of studies addressing cases involving CIs under seismic conditions. Four main observations can be made: First, the variation of bending with depth is not hydrostatic - in accord with available numerical studies.[11] Second, the maximum and minimum strain profiles are nearly symmetric, which provides evidence as to a certain degree of linearity in the backfill response and, thereby, justification as to the use of elastodynamic methods in relevant seismic earth pressure problems (Veletsos and Younan[67,89]). Third, bending at the top is small, which is in accord with the large value of the corresponding d_θ parameter (section 4.1) and provides evidence as to a limited expected amount of bending due to thermal action as well. Fourth, the bending strains in the wall are much lower than those in the piles (by over two orders of magnitude), which suggests that the body of the wall is not a critical region for the safety of the system.

Figure 13 presents the dynamic bending strain ε_p in the two instrumented piles, defined as $\varepsilon_p = M \cdot r/(E_p I_p)$, M being the bending moment, r the pile radius and E_p and I_p the pile's Young modulus and moment of inertia, respectively.[90] The figure shows the maximum and minimum ε_p on the East pile and West pile when subjected to test *S7* ground motion, versus dimensionless depth from ground surface, z/d. The maximum strains recorded by the sensor located at the top of the piles are shown in Figures 13A and 13C. The finite value of bending at the pile head in Figure 13A is due to the imperfect moment release given the presence of friction between the pile, and the stud yet is not considered significant enough to hinder the comparison between the 'released' and 'non-released' configurations. For the minimum moment (Figures 13B and 13D) similar observations can be made. In Figure 13B, the strains are 8.2, 6.7 and 10×10^{-3} for *noEPS*, *EPS1* and *EPS2*, respectively, in the connected pile (CP) configuration, while, when the pile heads are not connected, they drop to 1.3 and 1×10^{-3}. This highlights the beneficial role of pile head release in reducing bending moments. Yet, the transfer of seismic bending demand deep down the piles is not prevented by the head release (Figures 13B and 13D). Considering the 'active pile length' that is the length beyond which a pile behaves as an infinitely long flexural beam,[91,92] this is estimated to be around 0.2 m (10 pile diameters) that is, half the total length of the pile. Accordingly, any forces or movements acting at the pile tip do not affect the response at the pile head and vice versa. This feature of the response is supported by the near-zero bending at $z/d = 12$, which is expected to stay small all the way down to the pile tip given the hinged condition in that location.

By observing the strain profiles, a point of contraflexure appears close to the second strain gauge ($z/d = 3.15$, corresponding to $z = 0.07$ m); the maximum values of dynamic bending strains were recorded at $z/d = 9.9$, corresponding to $z = 0.22$ m. At 0.3 m from the top ($z/d = 13.5$), the strain is close to zero. This particular trend, both for noCP and CP configurations, is consistent with results from the literature.[90,93]

5.5 | Settlements

Settlement measurements seem to indicate a possible beneficial behaviour of the configuration with one layer of CI and connected piles. Measurements were performed manually in discrete locations on the backfill surface, so only

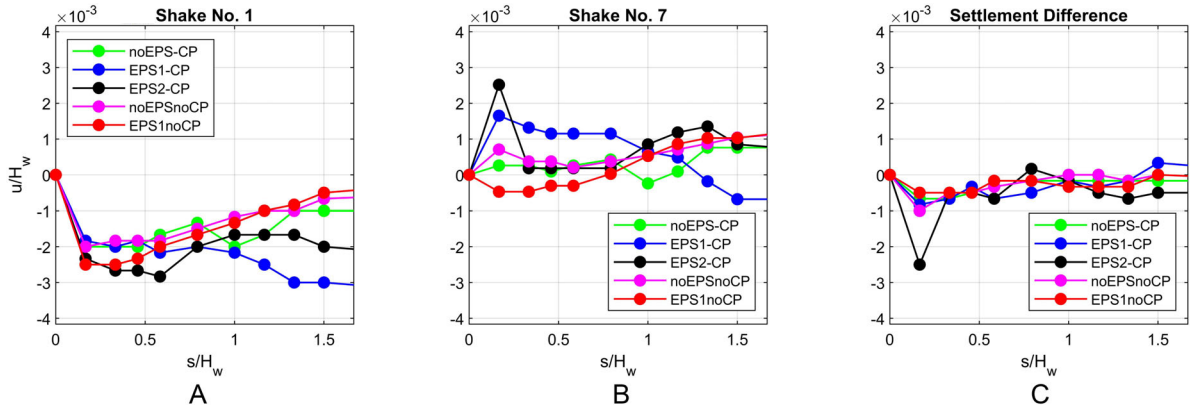

FIGURE 14 Backfill settlement following: A, shaking *S1*, B, shaking *S7* (Table 4) measured with respect to the deck height and C, settlement difference between the cases in (A) and (B). In all curves, settlement u and horizontal distance from the abutment s are normalised by the wall height H_w

indicative trends could be established. The measured settlements provide a lower bound of settlements at prototype scale given the high relative density (and thereby dilatant behaviour) of soil in the physical model. However, the comparison of the behaviour between the different configurations tested is valuable from a qualitative viewpoint. Figure 14 shows the settlement measured over a grid of 30 points along three lines on the backfill. The settlement observed after the *S1* event (Figure 14A) is indicative of the compressibility of the backfill against the horizontal restraint imposed by the CI or in its absence. Settlements are important for the design of IABs which can be useful for the design of transition slabs and for preventing road pavement damage.[96] The deformed soil profiles after *S1* demonstrate that the presence of CIs forces the backfill to expand laterally until equilibrium in the horizontal direction is achieved. The *EPS2-CP* configuration allows lateral ingress of sand towards the inclusion whereby the lost soil volume is compensated by backfill settlement. More significant results are obtained when the difference between settlements in each configuration is investigated (Figure 14C). Excluding the *EPS2-CP* case (i.e., the first configuration tested - Table 2), which looks like an outlier, the *EPS1-noCP* case seems the one with the smallest settlements.

6 | CONCLUSIONS

The work at hand reports on experimental results from a novel shaking table testing programme conducted on a physical model of an Integral Abutment Bridge (IAB) to investigate SSI effects between the bridge, the abutment, the backfill and the pile foundation, in presence/absence of compressive inclusions placed between the abutment wall and the backfill, as well as moment releases at the pile heads. Using a new set of similitude equations developed as part of this project, the bridge model was designed to fit the soil container at EQUALS laboratory, University of Bristol, and properly represent a prototype. The experimental campaign employed five different IAB configurations realised by (a) varying the number of Compressible Inclusion (CI) layers between the abutments and the backfill (no layers, one layer, two layers), (b) connecting or disconnecting the pile heads from the abutment footing (pile cap). Each configuration was subjected to a minimum of 13 different excitations involving a combination of white noise signals and recorded earthquake time histories from the Italian ground motion database. Over 75 tests were conducted in total, recorded by 64 data acquisition channels which generated 4800 time histories of data.

The following conclusions were drawn:

1. The analysis of the acceleration response in the free field array identified an amplification pattern from the bottom of the soil container to the ground surface, which was not affected by changes in the structural configuration and confirmed the undisturbed conditions aimed during the rig design.
2. The backfill accelerations consistently increase with increasing thickness of the CI (i.e., two layers versus one layer), due to the decrease in lateral restraint imposed by the abutment wall.
3. On the other hand, the accelerations on the bridge tend to decrease with the addition of CIs. The reduction is more pronounced for higher earthquake intensities, which suggests nonlinear soil behaviour. The beneficial effect of the CI is also evident at the base of the abutment wall, where a significant reduction in horizontal displacements was observed.

4. Disconnecting the pile heads from the abutment footing does not alter the horizontal wall displacements at the base, regardless of presence/absence of a CI.
5. The bending strains in the abutment wall decrease in presence of a CI. Disconnecting the pile heads from the footing further decreases bending in the abutment.
6. Bending strains in the piles are over two orders of magnitude higher than those in the abutment wall. This difference is expected to increase when a smaller number of piles (e.g. a single row) is employed. The release of pile heads from the footing is also effective in reducing bending near the pile head, yet it does not prevent development of bending deeper down the pile due to kinematic pile-soil interaction.
7. Some of the scaling laws adopted in the structural engineering literature, such as that for dynamic time, should not be used in SSI problems like the one at hand, as they do not account for the dependence of soil shear modulus on overburden pressure.
8. The levels of acceleration experienced by the bridge are not strong enough to induce failure in the backfill as the associated safety factors based on available limit-state solutions are in excess of 10. This justifies the use of linear/equivalent-linear procedures in the work at hand.

As a final remark, it is fair to mention that additional studies including an extensive numerical investigation would be needed to extend quantitatively all the results from model to prototype scale, overcome certain limitations of the experimental set up (including pile installation effects, variation in soil relative density, boundary effects in the soil box, details of bridge geometry) and explore configurations not considered in this campaign.

DATA AVAILABILITY STATEMENT

The data that support the findings of this study are available from the corresponding author upon reasonable request.

ACKNOWLEDGEMENTS

This research was conducted under the auspices of Seismic Response of Novel Integral Abutment-Bridges (SERENA) project, funded by the EU H2020 under grant agreement number 730900 (SERA), with George Mylonakis as Principal Investigator for University of Bristol. The authors gratefully acknowledge the DPC-ReLUIS consortium for the financial support within the framework of the 2014-2018 and 2019-2021 Research Projects, the National Natural Science Foundation of China (grant number: 51778148), Federbeton (Italy) for financial support for 'Seismic Behaviour of Integral Bridges', as well as the contribution of the personnel at EQUALS laboratory, University of Bristol. Finally, the authors would also like to thank Georgia De Benedetti and Francesco Lolli for their cooperation during the experimental campaign at the University of Bristol.

ORCID

Gabriele Fiorentino https://orcid.org/0000-0002-6444-0473
Cihan Cengiz https://orcid.org/0000-0002-9475-8124
Flavia De Luca https://orcid.org/0000-0003-2387-8580
George Mylonakis https://orcid.org/0000-0002-8455-8946
Dimitris Karamitros https://orcid.org/0000-0002-3185-7838
Matt Dietz https://orcid.org/0000-0002-1914-1060
Luiza Dihoru https://orcid.org/0000-0001-6971-195X
Davide Lavorato https://orcid.org/0000-0001-7753-1975
Bruno Briseghella https://orcid.org/0000-0002-8002-2298
Tatjana Isakovic https://orcid.org/0000-0002-7712-5931
Christos Vrettos https://orcid.org/0000-0002-3640-757X
Antonio Topa Gomes https://orcid.org/0000-0002-5149-8748
Anastasios Sextos https://orcid.org/0000-0002-2616-9395
Camillo Nuti https://orcid.org/0000-0002-0385-201X

REFERENCES

1. Rasulo A, Goretti A, Nuti C. Performance of lifelines during the the 2002 Molise, Italy, earthquake. *Earthq Spectra*. 2004;20(S1): S301-S314.
2. Nuti C, Rasulo A, Vanzi I, Seismic assessment of utility systems: application to water, electric power and transportation networks. Paper presented at: Proceedings of the Joint ESREL and SRA-Europe Conference - Safety, Reliability and Risk Analysis: Theory, Methods and Applications; September 22-25, 2008; Valencia, Spain.

3. Thoft-Christensen P. Infrastructures and life-cycle cost-benefit analysis. *Struct Infrastruct Eng*. 2012;8(5):507-516.
4. NIST. *Community Resilience Planning Guide for Buildings and Infrastructure Systems 2015, Volumes I and II*. Gaithersburg, MD: National Institute of Standards and Technology; 2016.
5. DesRoches R, Muthukumar S. Effect of pounding and restrainers on seismic response of multiple-frame bridges. *J Struct Eng*. 2007;128(7):860-869.
6. Assimaki D, Ledezma C, Montalva GA, Tassara A, Mylonakis G, Boroschek R. Site effects and damage patterns. *Earthq Spectra*. 2012;28(S1):S55-S74.
7. Dicleli M. Integral bridges. *Innovative Bridge Design Handbook*. Amsterdam, Netherlands: Butterworth-Heinemann; 2016.
8. Liang C, Liu Y, Zhao C, Lei B, Wu J. Experimental and numerical study on an innovative girder-abutment joint in composite bridges with integral abutments. *Constr Build Mater*. 2018;186:709-730.
9. Caristo A, Barnes J, Mitoulis SA. Numerical modelling of integral abutment bridges under seasonal thermal cycles. *Proc Inst Civil Eng – Bridge Eng*. 2018;171(3):179-190.
10. England GL, Bush DI, Tsang NC. *Integral Bridges: A Fundamental Approach to the Time-Temperature Loading Problem*. London, UK: Thomas Telford; 2000.
11. Mitoulis SA, Palaiochorinou A, Georgiadis I, Argyroudis S. Extending the application of integral frame abutment bridges in earthquake-prone areas by using novel isolators of recycled materials. *Earthq Eng Struct Dyn*. 2016;45(14):2283-2301.
12. Perić D, Miletić M, Shah BR, Esmaeily A, Wang H. Thermally induced soil structure interaction in the existing integral bridge. *Eng Struct*. 2016;106:484-494.
13. Burke MP, Jr. *Integral and Semi-Integral Bridges*. Chichester, UK: John Wiley & Sons; 2009.
14. Paraschos A, Amde AM. A survey on the status of use, problems, and costs associated with integral abutment bridges. *Better Roads*. 2011:1-20. http://www.betterroads.com/integral-abutment-bridges.
15. White H, Pétursson H, Collin P. Integral abutment bridges: the European way. *Pract Period Struct Des Constr*. 2010;15(3):201-208.
16. Bloodworth AG, Xu M, Banks JR, Clayton CR. Predicting the earth pressure on integral bridge abutments. *J Bridge Eng*. 2011;17(2):371-381.
17. Civjan SA, Kalayci E, Quinn BH, Breña SF, Allen CA. Observed integral abutment bridge substructure response. *Eng Struct*. 2013;56:1177-1191.
18. Dicleli M, Erhan S. Low cycle fatigue effects in integral bridge steel H-piles under earthquake induced strain reversals. *Advances in Structural Engineering*. New Delhi, India: Springer; 2015:2505-2512.
19. Dicleli M, Eng P, Albhaisi SM. Maximum length of integral bridges supported on steel H-piles driven in sand. *Eng Struct*. 2003;25(12):1491-1504.
20. Baptiste KT, Kim W, Laman JA. Parametric study and length limitations for prestressed concrete girder integral abutment bridges. *Struct Eng Int*. 2011;21(2):151-156.
21. Zordan T, Briseghella B, Lan C. Parametric and pushover analyses on integral abutment bridge. *Eng Struct*. 2011;33(2):502-515.
22. Zordan T, Briseghella B, Lan C. Analytical formulation for limit length of integral abutment bridges. *Struct Eng Int*. 2011;21(3):304-310.
23. BA 42/96. *The Design of Integral Bridges. Incorporating Amendment No.1 dated May 2003*. http://bailey.persona-pi.com/Public-Inquiries/M4-Newport/C%20-%20Core%20Documents/6.%20Transport%20and%20Engineering/DMRB/vol1/section3/ba4296.pdf.
24. Dhar S, Dasgupta K. Seismic soil structure interaction for integral abutment bridges: a review. *Transp Inf Geotech*. 2019;6(4):249-267.
25. BMVBS(Bundesministerium für Verkehr, Bau und Stadtentwicklung) Integrale Bauwerke. *RE-ING (Richtlinien für den Entwurf und die Ausbildung von Ingenieurbauten) Teil 2, Brücken, Abschnitt 5*. Berlin, Germany: BMVBS; 2013.
26. BSI PD 6694-1:2011. *Recommendations for the design of structures subject to traffic loading to BS EN 1997-1:2004*. London, UK: BSI; 2011.
27. Gaba A, Hardy S, Doughty L, Powrie W, Selemetas D. *Guidance on Embedded Retaining Wall Design*. London, UK: CIRIA; 2017.
28. Cole RT, Rollins KM. Passive earth pressure mobilization during cyclic loading. *J Geotec Geoenv*. 2006;132(9):1154-1164.
29. Buckle IG. *Seismic design issues for joint-less bridges with innovative integral abutments*. Reno, NV: Department of Civil and Environmental Engineering, University of Nevada Reno. http://jointlessbridges.fzu.edu.cn/attach/2017/02/20/255257.pdf.
30. Faraji S, Ting JM, Crovo DS, Ernst H. Nonlinear analysis of integral bridges: finite-element model. *J Geotech Geoenviron*. 2001;127(5):454-461.
31. Horvath JS, Integral-abutment bridges: problems and innovative solutions using EPS geofoam and other geosynthetics. *Res. Rpt. No. CE/GE-00*. 2000;2:1-152.
32. Horvath JS. *Integral-Abutment Bridges: Geotechnical Problems and Solutions Using Geosynthetics and Ground Improvement*. Morgantown, WV: West Virginia University; 2005.
33. Mylonakis G, Papantonopoulos KI, Chrysikos DA. New analytical solutions for retaining structures under static and dynamic loads. Paper presented at: XIV European Conference on Soil Mechanics and Geotechnical Engineering; September 24-27, 2007; Madrid, Spain.
34. Mylonakis G, Kloukinas P, Papantonopoulos C. An alternative to the Mononobe-Okabe equations for seismic earth pressures. *Soil Dyn Earthq Eng*. 2007;27(10):957-969.
35. Goel RK, Chopra AK. Evaluation of bridge abutment capacity and stiffness during earthquakes. *Earthq Spectra*. 1997;13(1):1-23.
36. McCallen DB, Romstad KM. Dynamic analyses of a skewed short-span box-girder overpass. *Earthq Spectra*. 1994;10(4):729-755.
37. Zhang J, Makris N. Seismic response analysis of highway overcrossings including soil-structure interaction. *Earthq Eng Struct Dyn*. 2002;31(11):1967-1991.
38. Kotsoglou A, Pantazopoulou S. Bridge-embankment interaction under transverse ground excitation. *Earthq Eng Struct Dyn*. 2007;36(12):1719-1740.

39. Kotsoglou AN, Pantazopoulou SJ. Assessment and modeling of embankment participation in the seismic response of integral abutment bridges. *Bull Earth Eng*. 2009;7(2):343.
40. Kappos AJ, Sextos AG. Seismic assessment of bridges accounting for nonlinear material and soil response, and varying boundary conditions. *Coupled Site and Soil-Structure Interaction Effects with Application to Seismic Risk Mitigation*. Dordrecht, Netherlands: Springer; 2009:195-208.
41. Itani AM, Peckan G. *Seismic Performance of Steel Plate Girder Bridges with Integral Abutments*. Washington, DC: Federal Highway Administration; 2011.
42. Wood JH. Earthquake design of bridges with integral abutments. Paper presented at: 6th International Conference on Earthquake Geotechnical Engineering; November 1-14, 2015; Christchurch, New Zealand.
43. Partos AM, Kazaniwsky PM. Geoboard reduces lateral earth pressures. Paper presented at: Geosynthetics 87, Industrial Fabrics Association International; February 24-25, 1987; New Orleans, LA.
44. McGown A, Andrawes KZ, Murray RT. Controlled yielding of the lateral boundaries of soil retaining structures. Paper presented at: Symposium on Geosynthetics for Soil Improvement; May 9, 1988; Nashville, Tennessee.
45. Bathurst RJ, Zarnani S, Gaskin A. Shaking table testing of geofoam seismic buffers. *Soil Dyn Earthq Eng*. 2007;27(4):324-332.
46. Athanasopoulos-Zekkos A, Lamote K, Athanasopoulos GA. Use of EPS geofoam compressible inclusions for reducing the earthquake effects on yielding earth retaining structures. *Soil Dyn Earthq Eng*. 2012;41:59-71.
47. Ertugrul OL, Trandafir AC, Yener Ozkan M. Reduction of dynamic earth loads on flexible cantilever retaining walls by deformable geofoam panels. *Soil Dyn Earthq Eng*. 2017;92:462-471.
48. Karpurapu R, Bathurst RJ. Numerical investigation of controlled yielding of soil-retaining wall structures. *Geotext Geomembranes*. 1992;11(2):115-131.
49. AbdelSalam SS, Azzam SA. Reduction of lateral pressures on retaining walls using geofoam inclusion. *Geosynth Int*. 2016;23(6):395-407.
50. Reddy SB, Krishna AM. Tyre chips as compressible inclusions in earth-retaining walls. *Proc Inst Civil Eng - Ground Improv*. 2017;170(3):137-148.
51. Saiidi M, Vosooghi A, Nelson R. Shake table studies of a four-span reinforced concrete bridge. *J Struct Eng*. 2013;139(8):1352-1361.
52. Wilson P, Elgamal A. Full-scale shake table investigation of bridge abutment lateral earth pressure. *Bull N Z Natl Soc Earthq Eng*. 2009;42(1):39-46.
53. Fiorentino G, Cengiz C, De Luca F, et al. Shaking Table tests on integral bridge model including soil-structure interaction. Paper presented at: Atti del XVIII Convegno ANIDIS; September 15-19, 2019; Ascoli Piceno, Italy.
54. Fiorentino G, Cengiz C, De Luca F, et al. Shaking table tests on an integral abutment bridge model: preliminary results. Paper presented at: COMPDYN 2019, 7th ECCOMAS Thematic Conference on Computational Methods in Structural Dynamics and Earthquake Engineering; June 24-26, 2019; Crete Island, Greece.
55. Pötzl M, Naumann F. Fugenlose betonbrücken mit flexiblen widerlagern. *Beton Stahlbetonbau*. 2005;100(8):675-685.
56. Prendergast LJ, Hester D, Gavin K. Development of a vehicle-bridge-soil dynamic interaction model for scour damage modelling. *Shock Vib*. 2016;2016: 1-15.
57. Crewe AJ, Lings ML, Taylor CA, Yeung AK, Andrighetto R. Development of a large flexible shear stack for testing dry sand and simple direct foundations on a shaking table in European Seismic Design Practice. *Balkema*. 1995;1:163-168.
58. Bhattacharya S, Lombardi D, Dihoru L, Dietz MS, Crewe AJ, Taylor CA. Model container design for soil-structure interaction studies. 2012;22:135-158.
59. Lings ML, Dietz MS. An improved direct shear apparatus for sand. *Géotechnique*. 2004;54(4):245-256.
60. Kloukinas P, Scotto di Santolo A, Penna A, et al. Investigation of seismic response of cantilever retaining walls: limit analysis vs shaking table testing. *Soil Dyn Earthq Eng*. 2015;77:432-445.
61. International Organization for Standardization.. *Geotechnical Investigation and Testing - Identification and Classification of Soil - Part 2: Principles for a Classification*. Geneva, Switzerland: ISO; 2017.
62. Kramer SL. *Geotechnical Earthquake Engineering*. Upper Saddle River, NJ: Prentice-Hall; 1996.
63. Duškov M. Materials research on EPS20 and EPS15 under representative conditions in pavement structures. *Geotext Geomembr*. 1997;15(1):147-181.
64. Hazarika H. Stress-strain modeling of EPS geofoam for large-strain applications. *Geotext Geomembr*. 2006;24(2):79-90.
65. Ossa A, Romo MP. Micro- and macro-mechanical study of compressive behaviour of expanded polystyrene geofoam. *Geosynth Int*. 2009;16(5):327-338.
66. Abdelrahman GE, Kawabe S, Tsukamoto Y, Tatsuoka F. Small-strain stress-strain properties of expanded polystyrene geofoam. *Soils Found*. 2008;48(1):61-71.
67. Veletsos AS, Younan AH. Dynamic response of cantilever retaining walls. *J Geotech Geoenviron*. 1997;123(2):161-172.
68. Psarropoulos PN, Klonaris G, Gazetas G. Seismic earth pressures on rigid and flexible retaining walls. *Soil Dyn Earth Eng*. 2005;25(7-10):795-809.
69. Horvath JS. Extended Veletsos-Younan model for geofoam compressible inclusions behind rigid, non-yielding earth-retaining structures. Paper presented at: Geotechnical Earthquake Engineering and Soil Dynamics IV. May 18-22, 2008; Sacramento, California.
70. Athanasopoulos GA, Nikolopoulou CP, Xenaki VC, Stathopoulou VD. Reducing the seismic earth pressures on retaining walls by EPS geofoam buffers - numerical parametric analysis. Paper presented at: Proceedings of 2007 Geosynthetics Conference; January 16-19, 2007; Washington DC.
71. Iai S. Similitude for shaking table tests on soil-structure-fluid model in 1g gravity field. *Soils Found*. 1989;29(1):105-118.

72. Towhata I. *Geotechnical Earthquake Engineering*. Berlin, Germany: Springer Science & Business Media; 2008.
73. Muir Wood D. *Geotechnical Modelling*. Cleveland, Ohio: CRC Press; 2014.
74. Harris HG, Sabnis G. *Structural Modeling and Experimental Techniques*. Cleveland, Ohio: CRC Press; 1999.
75. Iai S, Tobita T, Nakahara T. Generalised scaling relations for dynamic centrifuge tests. *Géotechnique*. 2005;55(5):355-362.
76. Chau KT, Shen CY, Guo X. Nonlinear seismic soil-pile-structure interactions: shaking table tests and FEM analyses. *Soil Dyn Earthq Eng*. 2009;29(2):300-310.
77. Durante MG, Di Sarno L, Mylonakis G, Taylor CA, Simonelli AL. Soil-pile-structure interaction: experimental outcomes from shaking table tests. *Earthq Eng Struct Dyn*. 2016;45(7):1041-1061.
78. Luzi L, Puglia R, Russo E. *ORFEUS WG5 Engineering Strong Motion Database, version 1.0. Istituto Nazionale di Geofisica e Vulcanologia, Observatories & Research Facilities for European Seismology*. 2016. http://doi:10.13127/ESM. Accessed December 16, 2016.
79. Italian Building Code. *Technical Recommendations for Buildings* – D.M. 17/01/2018. G.U. n.42 del 20/02/2018, NTC 2018. Italian Building Code: Rome, Italy; 2018.
80. De Luca F, Woods GE, Galasso C, D'Ayala D. RC infilled building performance against the evidence of the 2016 EEFIT Central Italy post-earthquake reconnaissance mission: empirical fragilities and comparison with the FAST method. *Bull Earth Eng*. 2017;16(7):2943-2969.
81. Fiorentino G, Forte A, Pagano E, et al. Damage patterns in the town of Amatrice after August 24th 2016 Central Italy earthquakes. *Bull Earthq Eng*. 2018;16(3):1399-1423.
82. Hashash YMA, Musgrove MI, Harmon JA, Groholski DR, Phillips CA, Park D. *DEEPSOIL 6.1. User manual*. Urbana, IL: Department of Civil and Environmental Engineering University of Illinois at Urbana-Champaign; 2016.
83. De Risi R, Penna A, Simonelli AL. Seismic risk at urban scale: the role of site response analysis. *Soil Dyn Earthq Eng*. 2019;123:320-336.
84. Seed HB, Wong RT, Idriss IM, Tokimatsu K. Modulii and damping factors for dynamic analyses for cohesionless soils. *J Geotech Eng*. 1986;112(11):1016-1032.
85. Chidichimo A, Cairo R, Dente G, Taylor CA, Mylonakis G. 1-g experimental investigation of bi-layer soil response and kinematic pile bending. *Soil Dyn Earthq Eng*. 2014;67:219-232.
86. Erhan S, Dicleli M. Parametric study on the effect of structural and geotechnical properties on the seismic performance of integral bridges. *Bull Earthq Eng*. 2017;15(10):4163-4191.
87. Khodair YA. Lateral earth pressure behind an integral abutment. *Struct Infrastruct Eng*. 2009;5(2):123-136.
88. Arsoy S. Mobilization of passive earth pressures behind abutments of jointless bridges. *Transp Res Rec*. 2004;1868(1):199-204.
89. Brandenberg SJ, Mylonakis G, Stewart JP. Kinematic framework for evaluating seismic earth pressures on retaining walls. *J Geotech Geoenviron Eng*. 2015;141(7):04015031.
90. Mylonakis G. Simplified model for seismic pile bending at soil layer interfaces. *Soils Found*. 2001;41(4):47-58.
91. Di Laora R, Rovithis E. Kinematic bending of fixed-head piles in nonhomogeneous soil. *J Geotech Geoenviron Eng*. 2015;141(4):04014126.
92. Karatzia X, Mylonakis G. Discussion of "kinematic bending of fixed-head piles in nonhomogeneous soil" by Raffaele Di Laora and Emmanouil Rovithis. *J Geotech Geoenviron Eng*. 2016;142(2):07015042.
93. Di Laora R, Mandolini A, Mylonakis G. Insight on kinematic bending of flexible piles in layered soil. *Soil Dyn Earthq Eng*. 2012;43:309-322.
94. Kloukinas P, Penna A, Scotto di Santolo AS, et al. Experimental investigation of dynamic behaviour of cantilever retaining walls. *Seismic Evaluation and Rehabilitation of Structures*. Cham, Switzerland: Springer; 2014:477-493.
95. SERENA. SERA-TA-INFRAIA-01-2016-2017 Research Infrastructure for Earthquake Hazard. 2020. https://sera-ta.eucentre.it/sera-ta-project-10/. Accessed March 30, 2020.
96. Dreier D, Burdet O., Muttoni A. Transition slabs of integral abutment bridges. *Structural engineering international*. 2011;21(2):144–150.

How to cite this article: Fiorentino G, Cengiz C, De Luca F, et al. Integral abutment bridges: Investigation of seismic soil-structure interaction effects by shaking table testing. *Earthquake Engng Struct Dyn*. 2021;50:1517–1538. https://doi.org/10.1002/eqe.3409